

**Light absorption by pollution, dust, and biomass burning aerosols:
A global model study and evaluation with AERONET measurements**

Mian Chin,¹ Thomas Diehl,^{1,2} Oleg Dubovik,³ Tom F. Eck,^{1,2} Brent N. Holben,¹ Aliaksandr Sinyuk,^{1,4} David G. Streets⁵

¹Laboratory for Atmospheres, NASA Goddard Space Flight Center, Greenbelt, Maryland, U.S.A.

²University of Maryland at Baltimore County, Baltimore, Maryland, U.S.A.

³Laboratoire d'Optique Atmospherique, Universite de Lille 1/CNRS, Villeneuve d'Ascq, Lille, France

⁴Science Systems and Applications, Inc., Lanham, Maryland, U.S.A.

⁵Argonne National Laboratory, Argonne, Illinois, U.S.A.

Corresponding author: Mian Chin, mian.chin@nasa.gov

Submitted to *Annales Geophysicae* for the special issue “From Deserts to Monsoons”

March 31, 2009

Abstract

Atmospheric aerosol distributions from 2000 to 2007 are simulated with the Goddard Chemistry Aerosol Radiation and Transport (GOCART) model to attribute light absorption by aerosol to its composition and sources from pollution, dust, and biomass burning. The 8-year, global averaged total aerosol optical depth (τ), absorption optical depth (τ_a), and single scattering albedo (ω) at 550 nm are estimated at 0.14, 0.0086, and 0.95, respectively, with sulfate making the largest fraction of τ (37%), followed by dust (30%), sea salt (16%), organic matter (OM) (13%), and black carbon (BC) (4%). BC and dust account for 43% and 53% of τ_a , respectively. From a model experiment with “tagged” sources, natural aerosols are estimated to be 58% of τ and 53% of τ_a , with pollution and biomass burning aerosols to share the rest. Comparing with data from the surface sunphotometer network AERONET, the model tends to reproduce much better the AERONET direct measured data of τ and α than its retrieved quantities of ω and τ_a . Relatively small in its systematic bias of τ for pollution and dust regions, the model tends to underestimate τ for biomass burning aerosols by 30-40%. The modeled α is 0.2 – 0.3 too low (particle too large) for pollution and dust aerosols but 0.2 – 0.3 too high (particle too small) for the biomass burning aerosols, indicating errors in particle size distributions in the model. Still, the model estimated ω is lower in dust regions and shows a much stronger wavelength dependence for biomass burning aerosols but a weaker one for pollution aerosols than those quantities from AERONET. These comparisons necessitate model improvements on aerosol size distributions, the refractive indices of dust and black carbon aerosols, and biomass burning emissions in order to better quantify the aerosol absorption in the atmosphere.

1. Introduction

Aerosol absorption in the atmosphere plays important roles in climate change. Aerosol radiative forcing is determined not only by the total amount of aerosol in the atmosphere but also by the abundance of the absorbing components (e.g., Hansen et al., 1997; Ackerman et al., 2000). Light-absorbing particles warm the atmosphere that offset the cooling effects by non-absorbing aerosols such as sulfate (IPCC 2007). The degree of aerosol-cloud-precipitation interaction critically depends on the absorbing aerosols, since they could change cloud fraction (Kaufman and Koren, 2006), cloud cover and cloud albedo (Hansen et al., 1997), atmospheric circulation, and precipitation pattern and duration (Menon et al., 2002; Kim et al., 2006; Lau et al., 2006). Furthermore, the absorption in the ultraviolet and shortwave visible solar spectral wavelengths can affect the atmospheric chemistry by altering the photodissociation rates for key oxidants (Dickerson et al., 1997; Martin et al., 2003; Bian et al., 2003).

Absorption of solar radiation in urban and biomass burning environments is attributed mainly to the presence of strong light absorbing carbonaceous aerosols, largely black carbon (BC), whereas in arid and semiarid regions and downwind mineral dust is a main absorbing species. The absorbing ability of aerosol species is determined by the imaginary part of the complex refractive index, which for BC is of two orders of magnitude higher than for dust (e.g., Kinne et al., 2003). However, the atmospheric mass loading of dust is also about two orders of magnitude higher than that of BC, making the total absorption in the solar spectrum comparable to BC.

Despite its importance, determining the effects of aerosol absorption remains difficult. Large uncertainty in the optical properties of absorbing aerosols proves to be a major factor. In most cases, the measurements of aerosol optical properties either are limited to particular source regions (e.g. Saharan dust) or confined to a small span of wavelength range (e.g., mid-visible), and, in some cases, have not been updated for decades. Yet, more complications occur when the particles are internally mixed with several aerosol components as the optical properties of such a mixture could be quite different from externally mixed particles (e.g., Jacobson, 2000; Stier et al., 2006; Schwarz et al., 2008). Another difficulty in quantifying the aerosol absorption arises from the large variability of aerosols. Unlike the long-lived greenhouse gases, such as carbon dioxide and methane, which have lifetimes from tens to hundreds of years, aerosols have short lifetimes ranging from less than one day to one or two weeks. The short lifetime combined with highly variable and often episodic absorbing aerosol sources, such as wind-blown dust and biomass burning, result in highly inhomogeneous distributions of absorbing aerosols in space and time.

Numerous observations of aerosol absorption have been conducted in several field experiments (see Bergstrom et al., 2007 for a summary), from surface based networks (e.g. Dubovik et al., 2002; Delene et al., 2002), and from satellite retrievals (Torres et al., 2005). Among them, the most comprehensive and probably the most accurate dataset is that from the ground-based sunphotometer network, the Aerosol Robotic Network (AERONET), which has been measuring total aerosol optical depth (τ) and retrieving aerosol single scattering albedo (ω) and aerosol absorption optical depth (τ_a) at multiple wavelengths for more than a decade worldwide. Nonetheless, while the AERONET data have been commonly used for satellite and model validations and for a wide range of aerosol research, they in fact lack vertical information, have limited coverage over ocean, and can only retrieve absorption information with sufficient accuracy in relatively high aerosol loading environments.

Keeping in mind both the necessities and difficulties involved in defining aerosol absorption, we present here global model simulated aerosol absorption with the Goddard Chemistry Aerosol

Radiation and Transport (GOCART) model from 2000 to 2007. Our purpose is to quantify the aerosol absorption in the atmosphere as a function of sources, regions, and spectral dependence for climate studies. We first describe the model components and how the absorption is calculated (section 2), then we evaluate the model simulated key aerosol parameters of τ , τ_a , ω , and the Ångström Exponent (α , indication of aerosol size) with the AERONET measurements/retrievals at different world regions (section 3). We then present the global distributions of these parameters and attribute them to the aerosol composition and to the origin of pollution, dust, and natural sources (section 4), followed by conclusions on major findings (section 5).

2. Model simulation of aerosol components and optical depth

The GOCART model uses assimilated meteorological fields from the Goddard Earth Observing System Data Assimilation System (GEOS DAS). In this study, the version 4 of GEOS DAS is used to drive an off-line simulation of global aerosols at a resolution of 2.5° longitude by 2° latitude and 30 vertical layers. Atmospheric processes include emission, chemistry, boundary layer mixing, advection, convection, dry and wet depositions, and hygroscopic growth of aerosol particles. Details of the GOCART model are described in our previous publications (Chin et al., 2000, 2002, 2004, 2007; Ginoux et al., 2001, 2004); a brief summary and recent updates are given below.

2.1. Anthropogenic and natural emissions

The aerosol simulation in GOCART from 2000 to 2007 includes major aerosol types of sulfate, dust, BC, organic carbon (OC), and sea salt, and the precursor gas species of SO_2 and dimethylsulfide (DMS). The model accounts for time-varying emissions from anthropogenic, biomass burning, biogenic, and volcanic sources, wind-blown dust, and sea salt. The annual anthropogenic emissions of SO_2 , BC, and OC between 2000 and 2006 (Streets et al., 2009) are used and they are estimated by considering more than 100 combinations of combustor technology, particle collection device, fuel type, and fuel use (Streets et al., 2004; Bond et al., 2004). Other anthropogenic emissions include the aircraft and ship emissions, which are interpolated or extrapolated from the available database (Eyring et al., 2005 for international ship emission, Mortlock et al., 1998 for aircraft emissions from the Atmospheric Effects of Aviation Project database). Biomass burning emissions of SO_2 , BC, and OC are calculated using the dry mass burned dataset from the Global Fire Emission Dataset version 2 (GFED v2) (van der Werf et al., 2003, 2006; Randerson et al., 2007) and the emission factors from Chin et al. (2004), which for BC and OC are 1 g kg^{-1} and 8 g kg^{-1} , respectively, that can be 40-100% higher than most commonly used values (Andreae and Merlet, 2001) but are within the observed range (see Chin et al., 2002). Volcanic emissions of SO_2 from sporadically erupting volcanoes are constructed from a combination of the Global Volcanism Program database (Siebert and Simkin, 2002-; <http://www.volcano.si.edu/world/>), satellite SO_2 data from the Total Ozone Mapping Spectrometer (TOMS) (Carn et al., 2003) and the Ozone Monitoring Instrument (OMI) (Krotkov et al., 2006; Carn et al., 2008), and in some cases from reported measurements near the volcanoes (Diehl et al., 2009). Emissions of SO_2 from continuously degassing volcanoes are from Andres and Kasgnoc (1998) and are assumed to be constant. The magnitude of volcanic eruption and volcanic SO_2 index (Bluth et al., 1997) are used to estimate the injection height, plume thickness, and the emitted SO_2 amount if not available from observations (Chin et al., 2000; Diehl et al., 2009). Dust and sea salt emissions with particle radius from 0.01 to $10 \mu\text{m}$ are

calculated instantaneously in the model as a function of surface winds and other conditions (Ginoux et al., 2001; Gong et al., 2003).

Figure 1 shows the annual emission from 2000 to 2007 of carbonaceous aerosols (BC and OC) from anthropogenic and biomass burning sources, SO₂ from anthropogenic and volcanic sources, dust, and sea salt. The anthropogenic, biomass burning, and dust emissions are divided into 7 world regions, roughly within North America (NAM), Europe (EUR), Asia (ASA), northern Africa and Middle East (NAF), South America (SAM), southern Africa (SAF), Australia/New Zealand/tropical Western Pacific countries (AUS) (domains shown in Figure 4). With the 2007 anthropogenic emission not yet available, this study uses the 2006 anthropogenic emission in the 2007 simulations. The anthropogenic carbonaceous aerosol emissions have a small, but steady increase from 2000 to 2006 for all regions, and the anthropogenic emission of SO₂ has also increased in most regions especially in Asia, but decreased in North America and kept nearly constant in Europe. The change in anthropogenic emission is a combined result of economic development and fuel-use efficiency in those regions. Biomass burning emissions, on the other hand, have large year-to-year variations in different regions where the differences can be more than a factor of 3 among the years, except in Africa (northern and southern) where the interannual variations are relatively small. The interannual variability of dust and sea-salt is small (within 3%), although regionally the variations are larger. Compared to other sources, volcanic emissions are more variable. The 8-year averaged emission rates of BC, OC, dust, sea salt, and sulfur (including gaseous phase SO₂ from anthropogenic, volcanic, biomass burning sources and DMS from ocean and particulate sulfate from anthropogenic sources) are shown in **Figure 2** as global maps; the mean value and the range of annual emissions are listed in **Table 1**.

2.2. Aerosol optical properties

The optical properties of sulfate, BC, OC, dust, and sea salt are based on the Optical Properties of Aerosols and Clouds (OPAC) (also known as Global Aerosol Dataset, Köpke et al., 1997; Hess et al., 1998); the size distributions and refractive indices used in our calculations are described in Chin et al. (2002) and listed here in **Table 2**. All aerosols except dust have different degree of hygroscopic growth under ambient conditions, which is parameterized as a function of relative humidity (Chin et al., 2002). The aerosol optical depth, τ , is calculated as $\tau_i = \beta_i M_d$ where the subscripts $i = \text{null}$ for total extinction optical depth, a for absorption and s for scattering optical depth, respectively; β is the mass extinction (or absorption, or scattering) cross-section ($\text{m}^2 \text{g}^{-1}$), also known as mass extinction (absorption, scattering) efficiency, and M_d is the dry aerosol mass load in g m^{-2} (see Chin et al. 2002 for more details). The property of aerosol absorption is often expressed with single scattering albedo ω , which is τ_s/τ : the lower the ω , the more the absorption. **Figure 3** illustrates the spectral-dependent quantities of β and ω of sulfate, BC, OC, sea salt, and dust at two different sizes. In the atmosphere, τ and ω depends on the absolute and relative abundance of different types of aerosols, respectively, as well as their hygroscopic growth. All aerosols are treated as external mixture in this study due to the difficulties in quantifying the mixing state and the resulting optical properties in our current capacity.

Figure 3 shows that the specific extinction β decreases with the increase of wavelength for sulfate, BC, and OC from 0.2 to 2 μm in wavelength but stays rather constant for coarse mode sea salt and dust. Small particles such as sulfate, BC, and OC are much more efficient in light extinction in the UV to visible wavelength than sea salt and dust (β values for these small particles are 5 to 10 times higher than dust and sea salt in the mid-visible). The major absorbing

aerosols in the UV to visible spectral range are dust and BC (right column, Figure 3). As wavelength increases, BC becomes more absorbing whereas dust becomes less absorbing. Meanwhile, OC also displays some absorbing ability at near UV but the ω becomes much lower in near IR. For the hygroscopic aerosols, the larger the particle size (because of larger RH), the more efficient the total extinction (higher β) but less absorbing because of higher water fraction in the aerosol particle; on the other hand, for dust aerosols which we consider as non-hygroscopic, the larger the particle size, the less efficient they are in total extinction albeit more absorbing.

The aerosol optical properties listed in Table 2 and Figure 3 however are subject to possible large uncertainties. Some recent studies have shown different values than what we used here, such as BC and dust refractive indices or single scattering albedo, but currently the OPAC dataset is the most comprehensive one in covering the optical properties in a wide spectral range from UV to infrared for different aerosol species. We first evaluate the model simulated τ and τ_a using the properties in Table 2 with the AERONET data, and the possible errors will be discussed in section 3.4.

3. Comparisons with AERONET data in world regions

3.1. AERONET

The AERONET program is a worldwide ground-based sun photometer network (Holben et al., 1998), which started in the early 1990s with more than a dozen sites and has since grown to include over 200 sites (<http://aeronet.gsfc.nasa.gov>). The automatic tracking sun and sky scanning radiometers make direct measurements of τ at 340, 380, 440, 500, 675, 870, 940, and 1020 nm (nominal wavelengths) during daytime, with an accuracy of ~ 0.01 - 0.02 . In addition, sky radiance measurements at 440, 675, 870, and 1020 nm (nominal wavelengths) in conjunction with the direct sun measured τ at these same wavelengths were used to retrieve aerosol size distributions and refractive indices, providing the spectral dependence of ω and τ_a (e.g. Dubovik and King, 2000; Dubovik et al., 2002, 2006). In this study, we use the version 2 AERONET τ , τ_a , and ω from 2000 to 2007, which is improved from the version 1 retrieved products (τ_a and ω) by accounting for the mixtures of spherical and non-spherical particle shapes and the better defined surface reflectance (Dubovik et al., 2006; Sinyuk et al., 2007; Eck et al., 2008). Because of the low sensitivity to the absorption when aerosol loading is low, τ_a and, in particular, ω are retrieved with sufficiently high accuracy only when the total τ at 440 nm is equal or higher than 0.4 and solar zenith angle is 50 degree or lower (Dubovik et al., 2000, 2002). Therefore the retrieved products, τ_a and ω , are much less available than the direct measurements of τ and limited in an environment with relatively high aerosol loading.

Aerosol particle sizes are commonly inferred from the spectral dependence of τ , expressed as the Ångström Exponent or α : $\alpha = -\log(\tau_1/\tau_2) / \log(\lambda_1/\lambda_2)$, where τ_1 and τ_2 are aerosol optical depth at wavelengths λ_1 and λ_2 , respectively. Smaller particles have stronger wavelength dependence (as illustrated in Figure 3) thus larger α . Since the dependence of $\log(\tau)$ on $\log(\lambda)$ is not strictly linear (e.g. Eck et al. 1999; also see Figure 3), the estimates of α may change with different selected wavelength ranges. Here we use the α determined from τ at 440 and 870 nm.

Figure 4 shows the location of the 173 AERONET sites that have at least 20 days of simultaneous data of both τ and τ_a at four wavelengths of 440, 675, 870, and 1020 nm during the 2000-2007 period. We further mark these sites with different colors according to their geographical locations in the 7 world regions described in section 2.1. These regions in general

have distinct characteristics: In NAM and EUR aerosols are mostly from pollutions sources, in NAF mostly dust, and in SAM and SAF mostly biomass burning aerosols. Aerosol composition is more diverse in ASA: dust in northwestern and northern central China, heavy pollution in eastern China and India, and pollution and biomass burning in southern part of ASA. Although there is also a variety of aerosol types in AUS region, such as biomass burning aerosols in northern Australia and Southeast Asia and dust in central and western Australia, it is the biomass burning aerosol that is the major component in the three AERONET sites located in the northern Australia (Figure 4).

3.2. Daily variations of AOD and optical properties in different aerosol regimes

Comparisons between AERONET and GOCART are shown in **Figure 5** on daily variations of τ , τ_a , ω (550 nm) and α (440-870 nm) at 8 selected sites from the 7 regions. The AERONET τ at 550 nm is interpolated from the measurements at 440 and 675 nm, using the logarithmic relationships between τ and λ (see section 3.1). To convert organic carbon to organic aerosols or organic matter (OM), we multiply the mass of OC by a factor of 1.4 (Malm et al., 1994; 2003) then report the value of OM optical depth thereafter. The aerosol composition from the model is plotted in different color shades in Figure 5a – 5h. Four statistical parameters that measure the degree of model performance against the AERONET data are also listed on each panel in Figure 5: correlation coefficient (R), relative or absolute mean bias (B_r for τ and τ_a and B_a for ω and α , respectively), root-mean-square error (E), and skill score (S) which is calculated as $S = 4(1+R)/[(\sigma_f+1/\sigma_f)^2(1+R_0)]$ where σ_f is the ratio of the standard deviation of model to that of observation and the R_0 is the maximum attainable R which is set to 1 (Taylor, 2001; see Chin et al., 2003 for more details in using it for model evaluation).

Over the GSFC site in the eastern U.S. (Figure 5a), the model indicates a predominant presence of sulfate aerosol for all seasons (top rows, Figure 5a), only perturbed by dust sporadically from the long-range transport. Although BC only has a very small fraction in total τ , it dominates τ_a at GSFC except in spring when τ_a of long-range transported dust is of similar magnitude. However, the model underestimates both τ and τ_a in the summer at GSFC. Both model and AERONET reveal similar seasonal variations of ω and α , with the highest value of both in the summer, meaning an increasing fraction of non-absorbing pollution aerosols (mostly sulfate) and a decreasing in aerosol particle size from winter to summer. Though closely reproducing the seasonal variation of α , the modeled values are typically 0.4 lower than the AERONET data (as shown in the B_a value on the last panel in Figure 5a). One might argue that the model may contain too much dust to bring the α down as our previous study on surface aerosol concentrations has shown that the model may have overestimated the fine mode dust at the surface (Chin et al., 2007); however, even if all the aerosols were sulfate, the α would only be about 1.7 (ref. Figure 3), still lower than the AERONET value near 2.0 in the summer season. We will discuss this in section 3.4.

Sulfate again is the dominant component of τ in Lille (Figure 5b) located at the north most part of France near the coast of North Sea. For its proximity to the North Sea, Lille can have a substantial fraction of sea salt aerosols in the winter when the winds are strong. The seasonal variation of aerosol composition is reflected in the change of α (bottom panel, Figure 5b) which is much lower in the winter than in the summer because of higher fraction of sea salt in the winter. The τ and τ_a exhibit large day-to-day variations from the model, which is also shown in the AERONET data although the retrieved τ_a are only available for a fraction of the time each

1 year. The modeled ω stays above 0.87 throughout whereas AERONET occasionally shows very
2 low ω (0.72 to 0.82; 3rd panel, Figure 5b). The modeled α is on average about 0.2 lower than the
3 AERONET value for Lille.

4 The model severely underestimates both τ and τ_a over Kanpur, India (Figure 5c, top two
5 panels), with values on average more than 60% lower than the AERONET data, especially in the
6 winter. Interestingly, the ω and α from the model agree with the AERONET data in both
7 seasonal variation and magnitude with little bias (Figure 5c, bottom two panels). Black Carbon is
8 the major absorbing component over Kanpur, but the seasonal variations of ω and α is regulated
9 by the relative abundance of dust and sulfate as the model suggested, both with significant
10 seasonal changes. The fact that the model has underestimated τ and τ_a but at the same time well
11 captured the ω and α implies that the model estimated fractions of each aerosol components are
12 probably correct but the magnitudes are not. Considering that dust and pollution come from
13 different locations to Kanpur (dust is mostly transported from the Thar Desert in India/Pakistan
14 in the west, pollution is mostly emitted locally) but have the same magnitude of bias, it is
15 possible that the underestimation of τ and τ_a by the model is a large-scale phenomenon, probably
16 due to the model resolution and/or the removal processes, not necessarily the wrong emissions.

17 In Beijing, China (Figure 5d), both τ and τ_a are considerably higher than those from other
18 pollution sites discussed previously (Figure 5a-5c), with daily maximum τ reaching 2.5 and τ_a
19 over 0.2 from the AERONET data. The model again significantly underestimates (about 40% on
20 average) the τ and τ_a over that site (top two panels, Figure 5d). In addition, AERONET data
21 show weak seasonal variations of τ whereas the model simulates a much stronger seasonal cycle.
22 Strong dust intrusion events occur regularly in the spring, which are reflected in the low α values
23 in both AERONET and the model (bottom panel, Figure 5d). However, the modeled pollution
24 level in the winter, most probably from the absorbing aerosols, is too low, causing much higher
25 ω and much lower α than AERONET. In this case, the emission of primary absorbing
26 carbonaceous aerosols or the secondary organic aerosols formed in the atmosphere from
27 pollution sources may have been significantly underestimated in the model. On the other hand, in
28 situ measurements in Beijing during the wintertime

29 Dust transported from the Sahara desert overwhelms both τ and τ_a over Cape Verde (Figure
30 5e), located right off the west coast of northern Africa, resulting in typical α values below 0.5. In
31 the wintertime, the site is influenced by the Sahel biomass burning, making a sharp increase of α
32 in the winter to above 1 (bottom panel, Figure 5e). The modeled τ on average agrees with the
33 AERONET data to within 10%, but the model overestimates τ_a by more than 50% on average.
34 The difference between AERONET and GOCART in the aerosol absorption is also reflected in
35 the ω : the modeled ω is 0.03 to 0.04 lower than that from the AERONET (3rd panel, Figure 5e).
36 This difference points to the dust optical properties in the model (Table 2), which is likely being
37 too absorbing.

38 The three Southern Hemispheric sites shown in Figure 5f to 5h, Alta Floresta in Brazil
39 (Figure 5f), Mongu in Zambia (Figure 5g), and Lake Argyle in Australia (Figure 5h), are mainly
40 dominated by biomass burning aerosol, with OM being the major aerosol component of τ and
41 BC the major component of τ_a . Although the seasonality is quite regular, as the fire activity
42 peaks in August to September over Alta Floresta and Mongu and a month later over Lake Argyle,
43 there are significant year-to-year variations of the fire intensity. For example, the average τ in
44 September 2007 in Alta Floresta is twice as high as that in the same month in 2000 from
45 AERONET. At the peak of biomass burning time, the model estimates a similar ω for all three

sites to be 0.82 to 0.85; this value appears to be too low for Alta Floresta but too high for Mongu and Lake Argyle as compared to AERONET data. The AERONET data thus suggest that the aerosol released from Mongu and Lake Argyle, mainly from the shrublands and savanna burning, is more absorbing than that released from Alta Floresta that is mainly from broadleaf forest burning. This difference between absorption of biomass burning aerosols in different regions has also been discussed in previous AERONET papers (e.g., Dubovik et al., 2002, Eck et al., 2003; Reid et al., 2005). The model does not account for the difference in BC to OM emission ratios in different biomass types, which would overestimate the absorption in Alta Floresta but underestimate the absorption in Mongu and Lake Argyle. Another difference between AERONET and GOCART is the particle size; the modeled α values are much larger (or particle sizes are much smaller) than the AERONET data over Alta Floresta in the non-burning period but agree with AERONET in Mongu. Some observations over the Amazon suggested the size of organic particles from the biogenic sources in Amazon can be much larger than that from pollution sources (J. V. Martins, personal communication, 2009), but the model does not make such a distinction.

3.2. Overall comparisons of τ , τ_a , ω , and α

The overall statistical comparisons between AERONET and GOCART at all 173 sites (Figure 4) during 2000 to 2007 are shown in **Table 3** for monthly and **Figure 6** for annual means of τ , τ_a , ω , and α . The minimum number of days with available AERONET data is 5 for calculating monthly means and 20 for annual means. The GOCART results are averaged over the same days for appropriate comparisons. These annual means in Figure 6 are color-coded for the 7 regions (Figure 4). Figure 6 shows that about 90% of model simulated annual averaged τ agree with AERONET within a factor of two, and on a global basis the modeled τ is about 8% lower than the AERONET data. The regions where modeled average τ is lower than AERONET by 30-40% are SAM, SAF, and AUS (Table 3), pointing to the likelihood of underestimated biomass burning emissions, as was noted in Figure 5. The comparison of τ_a , on the other hand, is more scattered, as only about 70% of the points are within a factor of 2 of agreement. There are also recognizable regional differences: modeled τ_a values are lower than AERONET at most sites located in pollution and biomass burning regions except SAM but are higher in dust dominated places (NAF and some sites in ASA), due to the overestimation of dust particle absorption (Figure 3).

With respect to ω , the modeled values for regions of NAM, EUR, and NAF are mostly confined within a narrow range (Figure 6), for example, 0.88 to 0.90 for NAF, 0.91 to 0.95 for Europe, and 0.94 to 0.96 for NAM, while the AERONET data for those regions exhibit a much wider spread. Table 3 shows that the largest discrepancies between model and AERONET are in NAF where modeled regional average ω is 0.03 lower (more absorbing) and in AUS where model is 0.06 higher (less absorbing) than AERONET.

The comparison of α separates the points into two groups, one below the 1:1 line (model being lower) and the other above (model being higher) (Figure 6). The model calculated α in EUR and NAF are almost exclusively lower than the AERONET observations, so as the majority points in NAM. Overall in these regions, α from the model is 0.2 – 0.3 lower than that from AERONET (Table 3). In contrast, modeled α in SAM, SAF, and AUS are almost exclusively higher than AERONET by 0.2 – 0.3 on average (Table 3). In ASA, the modeled α are higher at some of the sites but lower at others than that from AERONET; those points where model is

higher are dominated by biomass burning aerosols (e.g., Hua Hin, Mukdahan, Pimai in Thailand during burning season) and those where the model is lower are dominated by pollution and/or dust aerosols (e.g., Beijing and SACOL in China, Osaka in Japan, Dalanzadgad in Mongolia).

3.3. Spectral dependence of ω

We further examine in **Figure 7** the wavelength (λ) dependence of ω in the visible to shortwave infrared (440 – 1020 nm) spectral range at sites typically regarded as located in pollution, biomass burning, or dust in different regions, similar to that shown in Dubovik et al. (2002). For the four sites in pollution regions (GSFC, Lille, Kanpur, and Beijing, Figure 7a), both AERONET and GOCART show that in the visible spectral region, ω is the highest in GSFC among the four sites followed by Lille, and the lowest in Beijing and Kanpur. However, the spectral dependence from the model is weaker than that from AERONET, and the difference in ω increases at longer wavelengths. The AERONET retrieval and model simulation display different wavelength dependence of ω in Beijing and Kanpur: AERONET shows an increase of ω with λ in Kanpur but the model shows a decrease from mid-visible to shortwave infrared. On the other hand, the model exhibits an increase of ω with wavelength in Beijing, similar to the shape of dust sites (Figure 7c) but AERONET shows a convex shape with a maximum at 675 nm.

There are large differences in the ω - λ relationship between AERONET and GOCART at the four biomass burning sites (Figure 7b). AERONET displays a clear separation between forest burning (Bonanza Creek in Alaska and Alta Floresta in Brazil) and savanna/shrub burning (Mongu in Zambia and Lake Argyle in Australia): aerosols at Bonanza Creek and Alta Floresta are much less absorbing and have weaker wavelength dependence than those at Mongu and Lake Argyle. The model calculates a much stronger wavelength dependence of ω than AERONET at all four sites, although the model also shows that at Bonanza Creek aerosol is less absorbing and the wavelength dependence is weaker than at other biomass burning sites because of a higher sulfate fraction at that location, likely from the transport of pollutions from near (North America) and far (Europe and Asia) sources (Chin et al., 2007). The differences between AERONET and GOCART on these biomass burning sites have exposed a deficiency in the model on emission factors in different vegetation types, the particle size distributions, and the optical properties of biomass burning aerosols.

The model and AERONET display similar shapes of spectral dependence of ω over the four dust sites (Cape Verde and Blida in/near northern Africa, Solar Village in Saudi Arabia, Dalanzadgad in Mongolia) (Figure 7c), but the modeled ω is typically 0.02 to 0.03 lower than AERONET and behaves more similarly among the sites. Both model and AERONET show that the ω - λ relationship over Dalazadgad is different from other dust sites, but more so from AERONET data. Model component analysis shows that the sulfate fraction in Dalazadgad is higher than that at other sites, causing less increase of ω with wavelength.

3.4. Model evaluation and steps for improvement

The comparisons discussed above and shown in Figure 5 to Figure 7 have clearly revealed the similarities and differences in four key parameters, τ , τ_a , ω , and α between AERONET and GOCART. A summary of model evaluation is as follows:

- (1) Among the four parameters, best agreement between AERONET and GOCART are those directly measured by AERONET, namely τ and α , on regional and global scales (Table 3

and Figure 6). The model has a much lower skill in reproducing the AERONET retrieved quantities of ω and τ_a .

- (2) While the systematic bias of model calculated τ for pollution and dust regions is relatively small, the model systematically underestimate the τ for biomass burning aerosols by 30-40% in regions dominated by that type of aerosol, such as in South America, southern Africa, and Australia during the burning seasons. Considering the fact that we have used higher emission factors of carbonaceous aerosols than the commonly suggested values (e.g., Andreae and Merlet, 2001), our still-too-low biomass burning τ reveals the possibility that the dry mass burned estimates in GFED v2 may be too low, as other studies have also suggested (e.g., Bian et al., 2007).
- (3) There are clear differences between the model and AERONET on α . The modeled α is 0.2 – 0.3 too small (or the particles are too large) for pollution because the lognormal distribution sulfate particle size is probably too wide, and yet it is 0.2 – 0.3 too large (or the particles are too small) for the biomass burning aerosols because the effective radius of OM particles are probably too small. The α for dust from the model is also about 0.2 to 0.3 smaller than AERONET, suggesting too high a coarse mode fraction of dust.
- (4) The model estimated τ_a are generally lower than AERONET except in the dust dominated area of NAF. Over pollution-dominated areas the discrepancy indicates that the amount of absorbing aerosol, such as BC, is probably too low in the model. For biomass burning dominated areas, it is likely that the total emission is too low, since the τ values are also low there. The high bias of modeled dust τ_a is mostly the result of the incorrect optical properties used in the model (i.e. the imaginary part of the refractive index being too high, see Table 2), that is also shown in the values of ω .
- (5) The ω at 550 nm in the model for the dust dominated region of NAF is about 0.03 lower than that from AERONET with a much narrower range between different sites. It is thus possible that the optical property of dust used in model calculation is too absorbing, and the dust property is likely to be different at different locations. From AERONET the ω of forest biomass burning is much higher (less absorbing) than that from savanna/shrubland burning, reflecting the differences in smoke aerosol composition among different vegetation types. However the model does not take into account of those differences, resulting in more similar values of ω in different biomass burning regions.
- (6) The spectral dependence of ω in different aerosol regimes has shown that the model produces much stronger wavelength dependence for biomass burning aerosols but weaker for pollution aerosols than those from AERONET. This problem is related to the incorrect size distributions for sulfate and OM aerosols as discussed in (3).

These comparisons have provided multi-dimensional diagnostics of the shortcomings in the model as well as possible remedies for them. As just mentioned, the dust in the model on average is too absorbing (ω at 550 nm being 0.88 to 0.90 at the dust dominated sites) compared with AERONET, while other studies have reported a wide range of ω for dust. For example, some studies reported a relatively strong absorption by the Saharan dust with ω of 0.86 to 0.88 at mid-visible wavelength (Patterson et al., 1977), while others suggested a much weaker absorption of the same dust with a 550 nm ω value of about 0.97 (Kaufman et al., 2001), along with still other studies presenting ω values in between those numbers (Cattal et al., 2003; Bergstrom et al., 2007). Also, retrievals of Saharan dust refractive index based on TOMS or TOMS-AERONET combined observations found a much lower imaginary refractive index (less absorbing) in UV

wavelengths than the values archived in the OPAC (Colarco et al., 2002; Sinuyk et al., 2003). For models to incorporate the information from different measurements to calculate the dust absorption, it would require quantitative data of complex refractive indices that cover not only a single or a narrow range of wavelength(s) but also from UV to IR, at least for the solar spectral range. Such optical information should also be obtained from different geographical locations for different mineralogical compositions. A recent study that measures dust refractive index and ω from 300 to 1000 nm as a function of iron oxides contents (Lafon et al., 2006), for instance, would be suitable for our purpose albeit the need for extrapolations to longer wavelengths.

BC absorption in the model is another important area to improve. A recent review (Bond and Bergstrom, 2006) has suggested that the “light absorbing carbon”, which is mainly BC, should have a refractive index with higher values for both real and imaginary part ($1.85-0.71i$) at mid-visible wavelength and higher particle density (1.8 g cm^{-3}) than those compiled in the OPAC database (Table 2). Model simulations using the Bond-Bergstrom recommended values resulted in 40% increase of global averaged τ_a from the simulation using the OPAC optical properties (Stier et al., 2007), implying more than a factor of 2 increase over pollution and biomass burning regions (because dust absorption was not changed in the two simulations). Here, incorporating the Bond-Bergstrom recommended optical properties for BC in our model would likely improve the agreement between model and AERONET on τ_a even though it might worsen that on ω (Figure 3 and Table 6). Likewise, the mid-visible optical properties will have to be extrapolated to other wavelengths with larger uncertainties.

Sulfate and OM size distributions in the model should be modified. The comparisons of the 440-870 nm α at pollution and biomass burning sites (Figure 6) has made it clear that the wavelength dependence of sulfate is too weak and that of OM is too strong in the model compared to AERONET. It implies too large a size (or too broad a lognormal size distribution) for sulfate particles but too small a size (or too narrow a lognormal size distribution) for OM particles. The AERONET retrieved information on lognormal size distributions at pollution and biomass burning sites can help to refine the size distribution used in the Mie calculations to recalculate the wavelength-dependent mass extinction cross-sections.

Other aspects of model improvements enlightened from this study include considering the distinct biomass burning emission factors for BC and OM in different ecosystems, the differences in OM particle size between the combustions and biogenic sources, and biogenic emission amount.

4. Composition and origin of total and absorbing aerosols

With in mind the strengths and weaknesses of the model performance from the above evaluation, we present the model simulated global properties and estimated composition and origin as follows.

4.1. Global distributions of τ , τ_a , and ω and aerosol composition

Displayed in **Figure 8** are the model simulated climatology of τ , τ_a , and ω for January, April, July, October, and the total mean values averaged over the 8-year period from 2000 to 2007. Global averaged τ and τ_a at 550 nm are 0.14 and 0.0086, respectively, for this period. The highest τ and τ_a are located in regions and seasons with heavy loadings of dust, biomass burning, and pollution, such as northern Africa (mainly dust), northern and eastern China (mainly dust and pollution, respectively), and equatorial/southern hemispheric extra tropical land areas (mainly biomass burning). The lowest ω , or the highest absorbing fraction, is in the biomass

burning areas (tropical northern Africa in January, southern Africa in July), with values ranging from 0.84 to 0.88. Globally, τ and τ_a are the lowest in the NH winter (January) and the highest in the NH spring (April). However there is a large seasonal contrast between NH and SH. In the NH, the seasonal variation is mostly regulated by the dust and pollution transport while in the SH it is controlled by a strong seasonal cycle of biomass burning, although sea salt also plays a significant role in the southern ocean for τ . Global mean ω shows little variations in different seasons (0.94 to 0.96) but there are significant differences among regions, mainly controlled by the biomass burning.

The relative contributions of each aerosol component to τ and τ_a are shown in **Figure 9**. Globally, sulfate makes the largest fraction of τ (37%), followed by dust (30%), sea salt (16%), OM (13%), and BC (4%). Although BC is optically thin, it is an important component of aerosol absorption, accounting for 43% of τ_a while dust contributes to about 53%. Considering that the model may have overestimated τ_a in dust regions but underestimated that in biomass burning regions compared to AERONET (Figure 5 and Figure 6), we may expect a comparable amount of absorption from dust and BC if model agreed with AERONET better. The rest, 4% of τ_a , is from OM, which absorbs slightly in the visible wavelength (Figure 3). Note that these relative contributions are evaluated at the mid-visible wavelength of 550 nm. Because different aerosol species have different spectral variations of specific extinction β as well as ω (e.g., Figure 3 and Figure 7), these relative percentage numbers will change at different wavelengths.

Comparing with other model calculations, τ_a of BC from the GOCART model is considerably higher. In the recent multi-model experiments in the Aerosol Comparisons between Observations and Models (AeroCom) using fixed emissions, the τ_a of BC at 550 nm ranges from 0.0011 to 0.0035 among 9 global models with an average value of 0.0019 (Schulz et al., 2006). Similar value (0.0021) is given by the ECHAM model study using the OPAC optical properties for BC (Stier et al., 2007). Our study shows that the τ_a of BC at 550 nm is 0.0037, derived from total τ_a of 0.0086 (Figure 8, bottom right panel) and the percentage of BC contribution at 43.3% (Figure 9, top right panel). One of the major reasons for this difference is the emission: the total BC emission used in Schulz et al., 2006 and Stier et al., 2007 is 7.6 Tg yr⁻¹ (3.0 Tg yr⁻¹ biomass burning, 4.6 Tg yr⁻¹ fuel combustion, taken from Dentener et al., 2006), while it is 10.2 Tg yr⁻¹ (5.0 Tg yr⁻¹ biomass burning, 5.2 Tg yr⁻¹ fuel combustion, see Table 1) in our study.

4.2. Origin of total and absorbing aerosol

We further examine the origin of τ and τ_a from different sources of dust, biomass burning, and pollution. To do so, we have conducted two additional model simulations, one with biomass burning emissions of SO₂, BC, and OM turned off, and the other with natural sources only, i.e., excluding anthropogenic and biomass burning emissions. Aerosols from anthropogenic, biomass burning, and natural sources can then be derived from the standard simulation (with all sources) and the simulations with particular sources turned off. These simulations are conducted for 2007 only, when the composition percentages are within 1% as those in the 8-year climatology (Figure 9). The budget is listed in **Table 4** and also shown in **Figure 10**. Here we use the term “pollution” for aerosols from fuel combustions and “natural” for dust, sea salt, volcanic, and biogenic aerosols that include OM produced from terpene (emitted from vegetation) and sulfate from DMS (emitted from ocean) oxidations. We also assume that all dust aerosols are natural even though there is likely some “anthropogenic” dust from land use practices.

Not surprisingly, the highest percentages of τ for pollution, biomass burning, and natural aerosols are at the vicinities of their strongest source areas: NH mid-latitudes for pollution, tropical/SH subtropical regions for biomass burning, and deserts and remote ocean area for natural aerosols. Volcanic sources control the natural aerosol fraction in the tropical South Pacific (volcanic eruptions from Lopevi and Ambrym in the Vanuatu archipelago and Bagana in the Solomon Islands) and the South Indian Ocean east of Madagascar (eruption of Piton de la Fournaise volcano on Reunion Island), and to a smaller degree in the vicinity of Nicaragua and Costa Rica (degassing volcano Masaya and others). As we have shown in Figure 9, τ_a consists of mainly two components, dust and BC. Aerosol absorption is dominated by dust in the NH except over the pollution source areas, and by biomass burning aerosols in the SH except over the desert regions in Australia, Argentina, and Chile. Despite the proximity of boreal forest to the Arctic, biomass burning from boreal fire has limited impact on τ and τ_a in the Arctic (less than 10% for τ and 20% for τ_a on annual average), which is much weaker than the influence of the transport of pollution and dust aerosols. This is in part because the biomass burning is highly seasonal with relatively short duration, in contrast with the constantly available pollution and dust aerosols that are frequently making their way to the Arctic, especially in the winter and spring. Therefore the biomass burning impact to the Arctic is expected to be much larger during the burning season than the annual average. Globally, natural aerosols account for 58% of τ and 53% of τ_a , whereas pollution and biomass burning aerosols share the rest. If we assume biomass burning aerosols are mainly from anthropogenic activities, then the total anthropogenic fractions of global τ and τ_a are 42% and 47%, respectively.

5. Conclusions

We have reported our results from an 8-year (2000-2007) model simulation of atmospheric aerosols that quantifies aerosol absorption and attributes such absorption to aerosol composition and sources from pollution, dust, and biomass burning. The 8-year, global averaged τ , τ_a , and ω at 550 nm are estimated at 0.14, 0.0086, and 0.95, respectively. Sulfate makes the largest fraction of τ (37%) globally, followed by dust (30%), sea salt (16%), OM (13%), and BC (4%). Although BC is optically thin, it is an important component of aerosol absorption; it accounts for 43% of τ_a while dust contributes to about 53%. The rest, 4% of τ_a , is from OM. From a model experiment for 2007 in which the aerosol produced from pollution, biomass burning, and natural sources are “tagged”, we have found that the natural aerosols (dust, sea salt, volcanic, and biogenic) account for 58% of τ and 53% of τ_a , whereas pollution and biomass burning aerosols share the rest. If we assume biomass burning aerosols come mainly from anthropogenic activities, then the total anthropogenic fractions of global τ and τ_a are 42% and 47%, respectively. Given that the model may have overestimated τ_a in dust regions but underestimated that in pollution and biomass burning regions compared to data from the AERONET, we should expect a smaller difference in absorption from dust and anthropogenic aerosols globally. However, these quantities and their relative importance differ significantly with space and time, reflecting the high variability of sources and short lifetimes of aerosols. Also, these relative fractions at 550 nm will change at other wavelengths since different aerosols have different spectral dependence of mass extinction or absorption cross-sections (β or β_a).

We have compared the model results of τ , τ_a , ω , and α with those quantities measured or retrieved from the AERONET at 173 sites worldwide located in pollution, biomass burning, and dust regions. Among the four parameters, those match the best between AERONET and

GOCART are the ones directly measured by AERONET, namely τ and α , on regional and global scales. While the systematic bias of model calculated τ for pollution and dust regions is relatively small, the model usually underestimates the τ for biomass burning aerosols by 30-40%. This discrepancy suggests the possibility that the total dry mass burned from the current biomass burning emission dataset is much too low. The modeled size parameter, α , is 0.2 – 0.3 too low (or the particles are too large) for pollution as well as for dust aerosols but it is 0.2 – 0.3 too high (or the particles are too small) for the biomass burning aerosols, indicating errors in the size distributions of those aerosols used in model calculations.

The model has a much lower skill in reproducing the AERONET retrieved quantities of ω and τ_a . Compared with AERONET data, the model estimated τ_a is generally lower except in the dust dominated areas where the model is higher, and the modeled ω is lower for dust and forest burning areas but higher in savanna/shrubland burning places. These differences may be explained by a combination of several factors, including the incorrect optical properties for dust and carbonaceous aerosols, indiscriminative BC/OM emission factors for different burning vegetation types, and the likelihood of too low biomass burning emissions. The spectral dependence of ω in different aerosol regimes has shown that the model produces a much stronger wavelength dependence for biomass burning aerosols but a weaker one for pollution aerosols than those from AERONET, a problem that is related mainly to the incorrect size distributions for sulfate and OM aerosols used in the model.

The comparisons between GOCART and AERONET in this study have brought to the forefront the need for the model to incorporate the updated, knowledge based sulfate and OM size distributions, dust absorption properties as a function of iron composition, and BC refractive index. And the dry mass burned and trace gas and aerosol released from biomass burning will need to be further refined.

Because of the importance of aerosol absorption in the atmosphere, significant efforts should be undertaken to improve the predictive capability of models with particular respect to such a quantity. The evaluation of current models with satellite or AERONET data is mostly limited in its capacity to the mid-visible wavelength but, as this study has shown, such a comparison is not sufficient enough to evaluate the optical and microphysical properties in the model that are critical for climate studies. As more global model simulations now converge on the τ values at the mid-visible wavelength (e.g., Kinne et al., 2006 for multiple model studies in AeroCom), which is a result from considerable improvements of models to achieve a better agreement with that quantity from satellite and AERONET measurements, it is now necessary to expand the effort to evaluate the model performance at multi-wavelength and with multi-variables. Such effort will lead to further improved treatment of the chemical, physical, and optical properties in the models that will ultimately be used to assess the aerosol climate impacts of the past and project the climate response to the change of aerosols in the future.

Acknowledgment

The modeling work is supported by NASA Atmospheric Composition Modeling and Analysis Program (ACMAP), Modeling, Analysis and Prediction (MAP), EOS, and Radiation Science Program (RSP). The AERONET site managers and technical personnel are gratefully acknowledged. The NASA Grant Global Environmental Change-hazards and regional impacts (NNX06AF30G) and support from the technical officers Don Anderson and Lucia Tsaoussi are also acknowledged. In addition, we wish to thank Hongbin Yu for his comments on the manuscript.

References

- Ackerman, A. S., Toon, O. B., Stevens, D. E., Heymsfield, A. J., Ramanathan, V., Welton, E. J.: Reduction of tropical cloudiness. *Science*, 288, 1042-1047, 2000.
- Andreae, M. O., and Merlet, P.: Emission of trace gases and aerosols from biomass burning, *Global Biogeochem. Cycles*, 15, 955-966, 2001.
- Andres, R. J., Kasgnoc, A. D.: A time-averaged inventory of subaerial volcanic sulfur emissions, *J. Geophys. Res.*, 103(D19), 25251-25262, doi:10.1029/98JD02091, 1998.
- Bergstrom, R. W., Pilewskie, P., Russell, P. B., Redemann, J., Bond, T. C., Quinn, P. K., and Sierau, B.: Spectral absorption properties of atmospheric aerosols, *Atmos. Chem. Phys.*, 7, 5937-5943, 2007.
- Bian, H., Prather, M. J., and Takemura, T.: Tropospheric aerosol impacts on trace-gas budgets through photolysis, *J. Geophys. Res.*, 108, 4242, 2003.
- Bian, H., Chin, M., Kawa, S. R., Duncan, B., Arellano, A., and Kasibhatla, P.: Sensitivity of global CO simulations to uncertainties in biomass burning sources, *J. Geophys. Res.*, 112, D23308, doi:10.1029/2006JD008376, 2007.
- Bluth, G. J. S., Rose, W. I., Sprod, I. E., and Krueger, A. J.: Stratospheric loading of sulfur from explosive volcanic eruptions, *J. Geol.*, 105, 671-683, 1997.
- Bond, T. C., Streets, D. G., Yarber, K. F., Nelson, S. M., Woo, J.-H., and Klimont, Z.: A technology-based global inventory of black and organic carbon emissions from combustion, *J. Geophys. Res.*, 109, D14203, doi:10.1029/2003JD003697, 2004.
- Bond, T. C. and Bergstrom, R. W.: Light absorption by carbonaceous particles: An investigative review, *Aerosol Sci. Technol.*, 40, 27-67, 2006.
- Carn, S. A., Krueger, A. J., Bluth, G. S. J., Schaefer, S. J., Krotkov, N. A., Watson, I. M., and Datta, S.: Volcanic eruption detection by the Total Ozone Mapping Spectrometer (TOMS) instruments: A 22-year record of sulfur dioxide and ash emissions, in: *Volcanic Degassing*, Special Publication of the Geological Society of London, No. 213, edited by C. Oppenheimer, D. M. Pyle, and J. Barclay, 177-202, Geological Society, London, UK, 2003.
- Carn, S. A., Krueger, A. J., Arellano, S., Krotkov, N.A., and Yang, K.: Daily monitoring of Ecuadorian volcanic degassing from space, *J. Volcanol. Geotherm. Res.*, doi:10.1016/j.volgeores.2008.01.029, 2008.
- Cattal, C., Carder, K. L., and Gordon, H. R.: Columnar aerosol single-scattering albedo and phase function retrieved from sky radiance over the ocean: Measurements of Saharan dust, *J. Geophys. Res.*, 108, D9, 4287, doi:10.1029/2002JD002497, 2003.
- CCSP 2009: Atmospheric Aerosol Properties and Climate Impacts, A Report by the U.S. Climate Change Science Program and the Subcommittee on Global Change Research [Mian Chin, Ralph A. Kahn, and Stephen E. Schwartz (eds.)]. National Aeronautics and Space Administration, Washington, D.C., USA, 128 pp, 2009.
- Chin, M., Rood, R. B., Lin, S.-J., Müller, J.-F., and Thompson, A. M.: Atmospheric sulfur cycle simulated in the global model GOCART: Model description and global properties, *J. Geophys. Res.*, 105, 24671-24687, 2000.
- Chin, M., Ginoux, P., Kinne, S., Torres, O., Holben, B. N., Duncan, B. N., Martin, R. V., Logan, J. A., Higurashi, A., and Nakajima, T.: Tropospheric aerosol optical thickness from the GOCART model and comparisons with satellite and sun photometer measurements, *J. Atmos. Sci.*, 59, 461-483, 2002.

1 Chin, M., Ginoux, P., Lucchesi, R., Huebert, B., Weber, R., Anderson, T., Masonis, S., Blomquist, B.,
2 Bandy, A., and Thornton, D.: A global aerosol model forecast for the ACE-Asia field experiment, J.
3 Geophys. Res., 108(D23), 8654, doi:10.1029/2003JD003642, 2003.

4 Chin, M., Chu, D. A., Levy, R., Remer, L. A., Kaufman, Y. J., Holben, B. N., Eck, T., and Ginoux, P.:
5 Aerosol distribution in the northern hemisphere during ACE-Asia: Results from global model, satellite
6 observations, and sunphotometer measurements, J. Geophys. Res., 109, D23S90,
7 doi:10.1029/2004JD004829, 2004.

8 Chin, M., Diehl, T., Ginoux, P., and Malm, W.: Intercontinental transport of pollution and dust aerosols:
9 implications for regional air quality, Atmos. Chem. Phys., 7, 5501-5517, 2007.

10 Colarco, P. R., Toon, O. B., Torres, O., and Rasch, F. J.: Determining the UV imaginary part of refractive
11 index of Saharan dust particles from TOMS data and a three dimensional model of dust transport, J.
12 Geophys. Res., 107(D16), 10.1029/2001JD000903, 2002.

13 Delene, D. J., and Ogren, J. A.: Variability of aerosol optical properties at four North American surface
14 monitoring sites, J. Atmos. Sci., 59, 1135-1150, 2002.

15 Dentener, F., Kinne, S., Bond, T., Boucher, O., Cofala, J., Generoso, S., Ginoux, P., Gong, S.,
16 Hoelzemann, J., Ito, A., Marelli, L., Penner, J., Putaud, J.-P., Textor, C., Schulz, M., van der Werf, G.,
17 and Wilson, J.: Emissions of primary aerosol and precursor gases in the years 2000 and 1750, prescribed
18 data-sets for AeroCom, Atmos. Chem. Phys., 6, 4321-4344, 2006.

19 Dickerson, R. R., Kondragunta, S., Stenchikov, G., Civerolo, K. L., Doddridge, B. G., and Holben, B. N.:
20 The impact of aerosols on solar ultraviolet radiation and photochemical smog, Science, 278, 827-830,
21 1997.

22 Diehl, T., et al.: A global inventory of subaerial volcanic SO₂ emissions from 1979 to 2007, in preparation,
23 2009.

24 Dubovik, O., and King, M. D.: A flexible inversion algorithm for retrieval of aerosol optical proper-ties
25 from Sun and sky radiance measurements, J. Geophys. Res., 105, 20,673-20,696, 2000.

26 Dubovik, O., Smirnov, A., Holben, B. N., King, M. D., Kaufman, Y. J., Eck, T. F., and Slutsker, I.:
27 Accuracy assessments of aerosol optical properties retrieved from AERONET Sun and sky-radiance
28 measurements, J. Geophys. Res., 105, 9791-9806, 2000.

29 Dubovik, O., Holben, B. N., Eck, T. F., Smirnov, A., Kaufman, Y. J., King, M. D., Tanré, D., and
30 Slutsker, I.: Variability of absorption and optical properties of key aerosol types observed in worldwide
31 locations, J. Atmos. Sci., 59, 590-608, 2002.

32 Dubovik, O., Sinyuk, A., Lapyonok, T., Holben, B. N., Mishchenko, M., Yang, P., Eck, T. F., Volten, H.,
33 Munoz, O., Veihelmann, B., van der Zander, Sorokin, M., and Slutsker, I.: Application of light scattering
34 by spheroids for accounting for particle non-sphericity in remote sensing of desert dust, J. Geophys. Res.,
35 111, D11208, doi:10.1029/2005JD006619d, 2006.

36 Eck, T. F., Holben, B. N., Reid, J. S., Dubovik, O., Kinne, S., Smirnov, A., O'Neill, N. T., and Slutsker, I.:
37 The wavelength dependence of the optical depth of biomass burning, urban and desert dust aero-sols, J.
38 Geophys. Res., 104, 31,333-31,350, 1999.

39 Eck, T. F., Holben, B. N., Reid, J. S., O'Neill, N.T., Schafer, J. S., Dubovik, O., Smirnov, A., Yama-soe,
40 M.A., and Artaxo, P.: High aerosol optical depth biomass burning events: a comparison of optical
41 properties for different source regions, Geophys. Res. Lett., 30(20), 2035, doi:10.1029/2003GL017861,
42 2003.

1 Eck, T. F., et al.: Spatial and temporal variability of column-integrated aerosol optical properties in the
2 southern Arabian Gulf and United Arab Emirates in summer, *J. Geophys. Res.*, 113, D01204,
3 doi:10.1029/2007JD008944, 2008.

4 Eyring, V., H. Köhler, W., Van Aardenne, J., and Lauer, A.: Emissions from international shipping: 1.
5 The last 50 years, *J. Geophys. Res.*, 110, D17305, doi:10.1029/2004JD005619, 2005.

6 Ginoux, P., Chin, M., Tegen, I., Prospero, J., Holben, B., Dubovik, O., and Lin, S.-J.: Sources and
7 distributions of dust aerosols simulated with the GOCART model, *J. Geophys. Res.*, 106, 20225-20273,
8 2001.

9 Ginoux, P., Prospero, J., Torres, O., and Chin, M.: Long-term simulation of dust distribution with the
10 GOCART model: Correlation with the North Atlantic Oscillation, *Environ. Modeling and Software*, 19,
11 113-128, 2004.

12 Gong, S.: A parameterization of sea-salt aerosol source function for sub- and super-micron particles,
13 *Global Biogeochem. Cycles*, 17, 1097, doi:10.1029/2003GB002079, 2003.

14 Hansen, J., Sato, M., and Ruedy, R.: Radiative forcing and climate response, *Journal of Geophysical*
15 *Research*, 102, 6831-6864, 1997.

16 Hess, M., Köpke, P., and Schult, I.: Optical properties of aerosols and clouds: The software package
17 OPAC, *Bull. Amer. Meteorol. Assoc.*, 79, 831-844, 1998.

18 Holben, B. N., et al.: AERONET—A federated instrument network and data archive for aerosol
19 characterization, *Remote Sens. Environ.*, 66, 1–16., 1998.

20 IPCC, 2007: Changes in Atmospheric Constituents and in Radiative Forcing. In: *Climate Change 2007:*
21 *The Physical Science Basis*, Contribution of Working Group I to the Fourth Assessment Report of the
22 Intergovernmental Panel on Climate Change [Solomon, S., et al. (eds.)], Cambridge University Press,
23 Cambridge, UK, and New York, NY, USA, 2007.

24 Jacobson, M. Z.: A physically-based treatment of elemental carbon optics: Implications for global direct
25 forcing of aerosols, *Geophys. Res. Lett.*, 27, 217-220, 2000.

26 Kaufman, Y. J., Tanre, D., Dubovik, O., Karnieli, A., and Remer, L. A.: Absorption of sunlight by dust as
27 inferred from satellite and ground-based remote sensing, *Geophys. Res. Lett.*, 28, 1479-1483, 2001.

28 Kaufman, Y. J., and Koren, I.: Smoke and pollution aerosol effect on cloud cover, *Science*, 313, 655-658,
29 2006.

30 Kim, M.-K., Lau, W. K. M., Chin, M., Kim, K.-M., Sud, Y. C., and Walker, G. K.: Atmospheric
31 teleconnection over Eurasia induced by aerosol radiative forcing during boreal spring, *J. Climate*, 19,
32 4700-4718, 2006.

33 Kinne, S., et al.: Monthly averages of aerosol properties: A global comparison among models, satellite
34 data, and AERONET ground data, *J. Geophys. Res.*, 108(D20), 4634, doi:10.1029/2001JD001253, 2003.

35 Kinne, S., et al.: An AeroCom initial assessment – optical properties in aerosol component modules of
36 global models, *Atmos. Chem. Phys.*, 6, 1815-1834, 2006.

37 Köpke, P., Hess, M., Schult, I., and Shettle, E. P.: Global Aerosol Data Set. MPI Meteorologie Hamburg
38 Report No. 243, 44 pp., 1997.

39 Krotkov, N.A., Carn, S. A., Krueger, A.J., Bhartia, P.K., Yang, K.: Band residual difference algorithm for
40 retrieval of SO₂ from the AURA Ozone Monitoring Instrument (OMI), *IEEE Transactions on Geoscience*
41 *and Remote Sensing*, AURA special issue, 44(5), 1259-1266, doi:10.1109/TGRS.2005.861932, 2006.

1 Lafon, S., Sokolik, I. N., Rajot, J. L., Caquineau, S., and Gaudichet, A.: Characterization of iron oxides in
2 mineral dust aerosols: Implications for light absorption, *J. Geophys. Res.*, 111, D21207,
3 doi:10.1029/2005JD007016, 2006.

4 Lau, K.-M., and Kim, K.-M.: Observational relationship between aerosol and Asian monsoon circulation
5 rainfall, *Geophys. Res. Lett.*, 33, L21810, doi:10.1029/2006GL027546, 2006.

6 Malm, W. C., Sisler, J. F., Huffman, D., Eldred, R. A., and Cahill, T. A.: Spatial and seasonal trends in
7 particle concentration and optical extinction in the United States, *J. Geophys. Res.*, 99, 1347–1370, 1994.

8 Malm, W. C., Day, D. E., Kreidenweis, S. M., Collett, J. L., and Lee, T.: Humidity-dependent optical
9 properties of fine particles during the Big Bend Regional Aerosol Visibility Observational Study, *J.*
10 *Geophys. Res.*, 108(D9), 4279, doi:10.1029/2002JD002998, 2003.

11 Martin, R. V., Jacob, D. J., Yantosca, R. M., Chin, M., and Ginoux, P.: Global and regional decreases in
12 tropospheric oxidants from photochemical effects of aerosols, *J. Geophys. Res.*, 108, D3, 4097,
13 doi:10.1029/2002JD002622, 2003.

14 Menon, S., Hansen, J., Nazarenko, L., and Luo, Y.: Climate effects of black carbon aerosols in China and
15 India. *Science*, 297, 2250–2253, 2002.

16 Mortlock, A.M., and Van Alstyne, R.: Military, Charter, Unreported Domestic Traffic and General
17 Aviation 1976, 1984, 1992, and 2015 Emissions Scenarios, NASA/CR-1998-207639, 1998.

18 Patterson, E. M., Gillette, D. A., and Stockton, B. H.: Complex index of refraction between 300 and 700
19 nm for Saharan aerosols, *J. Geophys. Res.*, 82, 3153–3160, 1977.

20 Quinn, P. K., Miller, T. L., Bates, T. S., Ogren, J.A., Andrews, E., and Shaw, G. E.: A 3-year record of
21 simultaneously measured aerosol chemical and optical properties at Barrow, Alaska, *J. Geophys. Res.*,
22 107(D11), doi:10.1029/2001JD001248, 2002.

23 Randerson, J. T., van der Werf, G. R., Giglio, L., Collatz, G. J., and Kasibhatla, P. S.: Global Fire
24 Emissions Database, Version 2 (GFEDv2.1). Data set. Available on-line [<http://daac.ornl.gov/>] from Oak
25 Ridge National Laboratory Distributed Active Archive Center, Oak Ridge, Tennessee, U.S.A.
26 doi:10.3334/ORNLDAAAC/849, 2007.

27 Reid, J. S., Eck, T. F., Christopher, S. A., Koppmann, R., Dubovik, O., Eleuterio, D., Holben, B. N., Reid,
28 E. A., and Zhang, J.: A Review of biomass burning emissions part III: Intensive optical properties of
29 biomass burning particles, *Atmos. Chem. Phys.*, 5, 827-849, 2005.

30 Schulz, M., Textor, C., Kinne, S., Balkanski, Y., Bauer, S., Bernsten, T., Berglen, T., Boucher, O.,
31 Dentener, F., Guibert, S., Isaksen, I., Iversen, T., Koch, D., Kirkevåg, A., Liu, X., Montanaro, V., Myhre,
32 G., Penner, J., Pitari, G., Reddy, S., Seland, Ø., Stier, P., and Takemura, T.: Radiative forcing by aerosols
33 as derived from the AeroCom present-day and pre-industrial simulations, *Atmos. Chem. Phys.*, 6, 5225–
34 5246, 2006.

35 Schwarz, J. P., et al., Coatings and their enhancement of black carbon light absorption in the tropical
36 atmosphere, *JGR* 113, D03203, doi:10.1029/2007JD009042, 2008.

37 Siebert, L., and Simkin, T.: *Volcanoes of the World: an Illustrated Catalog of Holocene Volcanoes and*
38 *their Eruptions*. Smithsonian Institution, Global Volcanism Program Digital Information Series, GVP-3,
39 2002.

40 Stier, P., Seinfeld, J. H., Kinne, S., Feichter, J., and Boucher, O.: Impact of nonabsorbing anthropogenic
41 aerosols on clear-sky atmospheric absorption, *J. Geophys. Res.*, 111, D18201,
42 doi:10.1029/2006JD007147, 2006.

43 Stier, P., Seinfeld, J. H., Kinne, S., and Boucher, O.: Aerosol absorption and radiative forcing, *Atmos.*
44 *Chem. Phys.*, 7, 5237-5261, 2007.

1 Sinyuk, A., Torres, O., Dubovik, O.: Combined use of satellite and surface observations to infer the
2 imaginary part of refractive index of Saharan dust, *Geophys. Res. Lett.*, 30, 10.1029/2002GL016189,
3 2003.

4 Sinyuk, A., et al.: Simultaneous retrieval of aerosol and surface properties from a combination of
5 AERONET and satellite, *Remote Sens. Environ.*, 107, 90– 108, doi:10.1016/j.rse.2006.07.0222007, 2007.

6 Streets, D. G., Bond, T. C., Lee, T., and Jang, C.: On the future of carbonaceous aerosol emissions, *J.*
7 *Geophys. Res.*, 109, D24212, doi:10.1029/2004JD004902, 2004.

8 Streets, D. G., Yan, F., Chin, M., Diehl, T., Mahowald, N., Schultz, M., Wild, M., Wu, Y., and Yu, C.:
9 Discerning human and natural signatures in regional aerosol trends, 1980-2006, submitted to *J. Geophys.*
10 *Res.*, 2009.

11 Tayler, K. E.: Summarizing multiple aspects of model performance in a single diagram, *J. Geophys. Res.*,
12 106, 7183– 7192, 2001.

13 Torres, O., Bhartia, P. K., Sinyuk, A., Welton, E. J., and Holben, B.: Total Ozone Mapping Spectrometer
14 measurements of aerosol absorption from space: Comparison to SAFARI 2000 ground-based
15 observations, *J. Geophys. Res.*, 110, D10S18, doi:10.1029/2004JD004611, 2005.

16 van der Werf, G. R., Randerson, J. T., Collatz, G. J., and Giglio, L.: Carbon emissions from fires in
17 tropical and subtropical ecosystems, *Global Change Biol.*, 9, 547–562, 2003.

18 van der Werf, G. R., Randerson, J. T., Giglio, L., Collatz, G. J., Kasibhatla, P. S., and Arellano, A. F., Jr.:
19 Interannual variability in global biomass burning emissions from 1997 to 2004, *Atmos. Chem. Phys.*, 6,
20 3424-3441, 2006.

Table 1. Aerosol and precursor emissions averaged from 2000 to 2007.

Species / Source	8-year avg. Emission (TgM yr ⁻¹) [§]	Range (TgM yr ⁻¹) [§]
BC	10.2	
Pollution	5.2	4.8 – 5.5
Biomass burning	5.0	4.5 – 5.3
OC	61.8	
Pollution	8.9	8.5 – 9.2
Biomass burning	40.2	36.1 – 42.3
Biogenic [#]	12.7	--
Sulfur [*]	93.6	
Pollution	65.5	60.2 – 70.2
Biomass burning	2.8	2.9 – 3.0
Volcanic	10.2	7.4 – 12.8
DMS	15.1	14.8 – 15.4
Dust	3250	3060 – 3340
Sea salt	5060	4920 – 5140

[§] Emission rate in TgM yr⁻¹ where M is C for BC and OC and S for sulfur emissions.

^{*} Sulfur emission including SO₂ emissions from pollution, biomass burning, and volcanic sources, a small fraction (3%) of sulfate from anthropogenic sources, and DMS from the ocean.

[#] Biogenic OC source is the conversion of terpene emitted from vegetation to organic aerosol. We use the same terpene emission from Guenther et al., 1997 for every year.

Table 2. Particle density (ρ), modal and effective radii (r_m and r_e), geometric standard deviation (σ_g) in lognormal size distribution, and refractive indices at 550 nm for dry aerosols.

Species	ρ (g cm ⁻³)	r_m (μm)	r_e (μm)	σ_g (μm)	Refractive index at 550 nm
BC*	1.0	0.0118	0.039	2.00	$1.75 - 0.44i$
OC*	1.8	0.0212	0.087	2.20	$1.53 - 0.006i$
Sulfate*	1.7	0.0695	0.156	2.03	$1.43 - 10^{-8}i$
Dust	2.6	0.0421	0.14	2.00	$1.53 - 0.0055i$
	2.6	0.0722	0.24	2.00	$1.53 - 0.0055i$
	2.6	0.1354	0.45	2.00	$1.53 - 0.0055i$
	2.6	0.2407	0.80	2.00	$1.53 - 0.0055i$
	2.6	0.4212	1.40	2.00	$1.53 - 0.0055i$
	2.6	0.7220	2.40	2.00	$1.53 - 0.0055i$
	2.6	1.3540	4.50	2.00	$1.53 - 0.0055i$
	2.6	2.4070	8.00	2.00	$1.53 - 0.0055i$
Sea salt	2.2	0.228	0.80	2.03	$1.50 - 10^{-8}i$
	2.2	1.64	5.73	2.03	$1.50 - 10^{-8}i$

* Assuming maximum radius at 0.5 μm.

Table 3. Statistics of AERONET-GOCART comparisons of monthly mean[§] 550 nm τ , τ_a , and ω and 440-870 nm α for seven world regions as well as for all sites from 2000 to 2007. See Figure 4 for region domains.

Region	Statistical Quantity*			
τ :	R	B_r	E	S
NAM	0.509	0.907	0.098	0.543
EUR	0.440	1.120	0.091	0.718
ASA	0.459	0.759	0.245	0.594
NAF	0.650	1.135	0.198	0.825
SAM	0.769	0.638	0.198	0.866
SAF	0.851	0.613	0.114	0.729
AUS	0.837	0.675	0.071	0.585
ALL	0.685	0.959	0.154	0.834
τ_a :	R	B_r	E	S
NAM	0.120	0.440	0.021	0.096
EUR	0.183	0.709	0.016	0.591
ASA	0.227	0.634	0.035	0.570
NAF	0.342	1.461	0.036	0.554
SAM	0.527	0.952	0.046	0.372
SAF	0.793	0.470	0.037	0.811
AUS	0.497	0.324	0.046	0.536
ALL	0.331	0.940	0.032	0.615
ω :	R	B_a	E	S
NAM	0.455	-0.005	0.036	0.560
EUR	0.189	0.002	0.030	0.372
ASA	0.533	-0.004	0.030	0.721
NAF	0.140	-0.032	0.044	0.181
SAM	0.498	-0.022	0.045	0.746
SAF	0.677	0.010	0.027	0.698
AUS	0.531	0.058	0.063	0.540
ALL	0.468	-0.014	0.037	0.679
α :	R	B_a	E	S
NAM	0.629	-0.301	0.394	0.790
EUR	0.583	-0.356	0.411	0.790
ASA	0.655	-0.246	0.395	0.697
NAF	0.802	-0.202	0.284	0.855
SAM	0.666	0.218	0.318	0.832
SAF	0.905	0.245	0.311	0.777
AUS	0.770	0.318	0.363	0.811
ALL	0.784	-0.225	0.371	0.891

[§] Monthly mean is obtained by averaging the available AERONET data in a particular month (minimum 5 days). GOCART monthly mean is calculated for the same days when AERONET data are available.

* R =correlation coefficient, B_r = relative mean bias (for τ and τ_a), B_a =absolute mean bias (for ω and α), E =root-mean-square error, S =skill score (see text and Figure 5a caption for explanation).

Table 4. Aerosol composition, origin, and the relative contribution to τ and τ_a at 550 nm for 2007. Numbers in parenthesis are global averages.

Species / Origin	τ (0.14)	τ_a (0.0090)
BC	3.8%	43.9%
Pollution	1.9%	21.8%
Biomass burning	1.9%	22.1%
OM	13.3%	3.8%
Pollution	2.0%	0.6%
Biomass burning	9.8%	2.9%
Natural*	1.5%	0.4%
Dust	30.7%	52.3%
Sulfate	36.1%	
Pollution	23.6%	
Biomass burning	2.6%	
Natural*	10.0%	
Sea salt	16.0%	
Total pollution	27.5%	22.3%
Total biomass burning	14.3%	25.0%
Total Natural*	58.2%	52.7%

* Natural OM aerosol including those formed from oxidation of terpene emitted from vegetations. Natural sulfate aerosol including sulfate formed from dimethyl sulfide (emitted from the ocean) and SO₂ from volcanic eruptions. These aerosols plus dust and sea salt constitute total natural aerosols.

Figure captions

Figure 1. Emissions of aerosols and precursor gases from their major sources and source regions from 2000 to 2007, annual total amount. NAM = North America, EUR = Europe, ASA = Asia, NAF = northern Africa and Middle East, SAM = South America, SAF = southern Africa, AUS = Australia/New Zealand and countries in the tropical South Pacific. See Figure 4 for region domains.

Figure 2. 8-year (2000-2007) averaged emission rates of BC, OC, dust, sea salt, and sulfur from all (including anthropogenic, biogenic, volcanic, biomass burning, and oceanic) sources. Emission of sulfur includes gaseous phase SO_2 and DMS and particulate sulfate emissions.

Figure 3. Mass extinction cross-section (aka mass extinction efficiency) β (left column) and single scattering albedo ω (right column) for sulfate, BC, OC, coarse sea salt, and dust as a function of wavelength from 250 to 2000 nm. Four different sizes of each species are shown with respective effective radius (r_e) at different RH values indicated in the panels in the right column.

Figure 4. AERONET site locations where simultaneous τ and τ_a data are available for at least 20 days during 2000 to 2007 (total 173 sites). Eight sites in white circles are selected for detailed analysis shown in Figure 5 (GSFC, USA, 40.0°N, 76.8°W; Lille, France, 51.6°N, 3.1°E; Kanpur, India, 26.5°N, 80.2°E; Beijing, China, 40.0°N, 116.4°E; Cape Verde, Sal Island, 16.7°N, 22.9°W; Alta Floresta, Brazil, 9.9°S, 56.1°W; Mongu, Zambia, 15.3°S, 21.2°E; Lake Argyle, Australia, 16.1°S, 128.8°E). These sites together with another four sites in white squares (Bonanza Creek, USA, 64.7°N, 148.3°W; Blida, Algeria, 36.5°N, 2.9°E; Solar Village, Saudi Arabia, 24.9°N, 46.4°E; Dalanzadgad, Mongolia, 43.6°N, 104.4°E) are used for the spectral dependence analysis of ω in Figure 7.

Figure 5a. Daily aerosol optical depth (τ , 1st panel), absorption optical depth (τ_a , 2nd panel), single scattering albedo (ω , 3rd panel) at 550 nm and Ångström exponent derived from τ at 440-870 nm (α , last panel) at Goddard Space Flight Center (GSFC) in eastern U.S.A. In the first two panels, GOCART aerosol components accumulated to total amount are shown in shaded color with DU=dust, BC=black carbon, OM=organic matter, SU=sulfate, and SS=sea salt. In the last two panels, model values are shown blue line with GO=GOCART. On each panel, R =correlation coefficient, B =bias with B_r in first two panels as relative mean bias, i.e. $\Sigma(\text{GOCART}_i)/\Sigma(\text{AERONET}_i)$ and B_a in the last two panels as absolute bias, i.e. $\Sigma(\text{GOCART}_i - \text{AERONET}_i)/n$ (n =total number of observations), E =root-mean-square error, and S =skill score. See text (section 3.2) for calculation of S .

Figure 5b. Same as Figure 5a but for Lille, France.

Figure 5c. Same as Figure 5a but for Kanpur, India.

Figure 5d. Same as Figure 5a but for Beijing, China.

Figure 5e. Same as Figure 5a but for Cape Verde, off the west coast of northern Africa.

Figure 5f. Same as Figure 5a but for Alta Floresta in Brazil.

Figure 5g. Same as Figure 5a but for Mongu, Zambia.

Figure 5h. Same as Figure 5a but for Lake Argyle in Australia.

Figure 6. Overall comparisons of τ , τ_a , and ω at 550 nm and α at 440-870 nm between AERONET and GOCART at all 173 AERONET sites (see Figure 3) during 2000-2007. Each point represents the annual average of the available AERONET data with a year. Model output is averaged for the same days. Points are color coded according to the regions (see Figure 3). 1:1 ratio in dashed line and 2:1 in dotted lines on τ and τ_a panels. Statistical variables on each panel are: R =correlation coefficient, B_r =relative mean bias (for τ and τ_a), B_a =absolute mean bias (for ω and α), E =root-mean-square error, and S =skill score. See text and Figure 5a caption for explanations.

Figure 7. Spectral dependence of ω at four sites each located at (a) pollution, (b) biomass burning, and (c) dust regions as shown in the AERONET retrieval (top row) and GOCART model (bottom row). Points are averaged over all available daily data from AERONET retrievals from 2000 to 2007. Site locations are indicated in Figure 4 and discussed in the text.

Figure 8. Global distributions of τ (left column), τ_a (middle column), and ω (right column) in January (1st row), April (2nd row), July (3rd row), and October (4th row) averaged over 8-year period from 2000 to 2007. The time averages of τ , τ_a , and ω for the entire 8-year period are shown in the last row.

Figure 9. Left column: Percentage contributions to 550 nm τ from BC, OM, dust, sea salt, and sulfate. Right column: same as the left column but for τ_a . Sea salt and sulfate are not shown in the right column because of their zero contributions to τ_a .

Figure 10. Percentage contributions to 550 nm τ (left column) and τ_a (right column) from pollution (top row), biomass burning (middle row), and natural (bottom row) aerosols in 2007. Natural aerosol including dust, sea salt, biogenic, and volcanic aerosols.

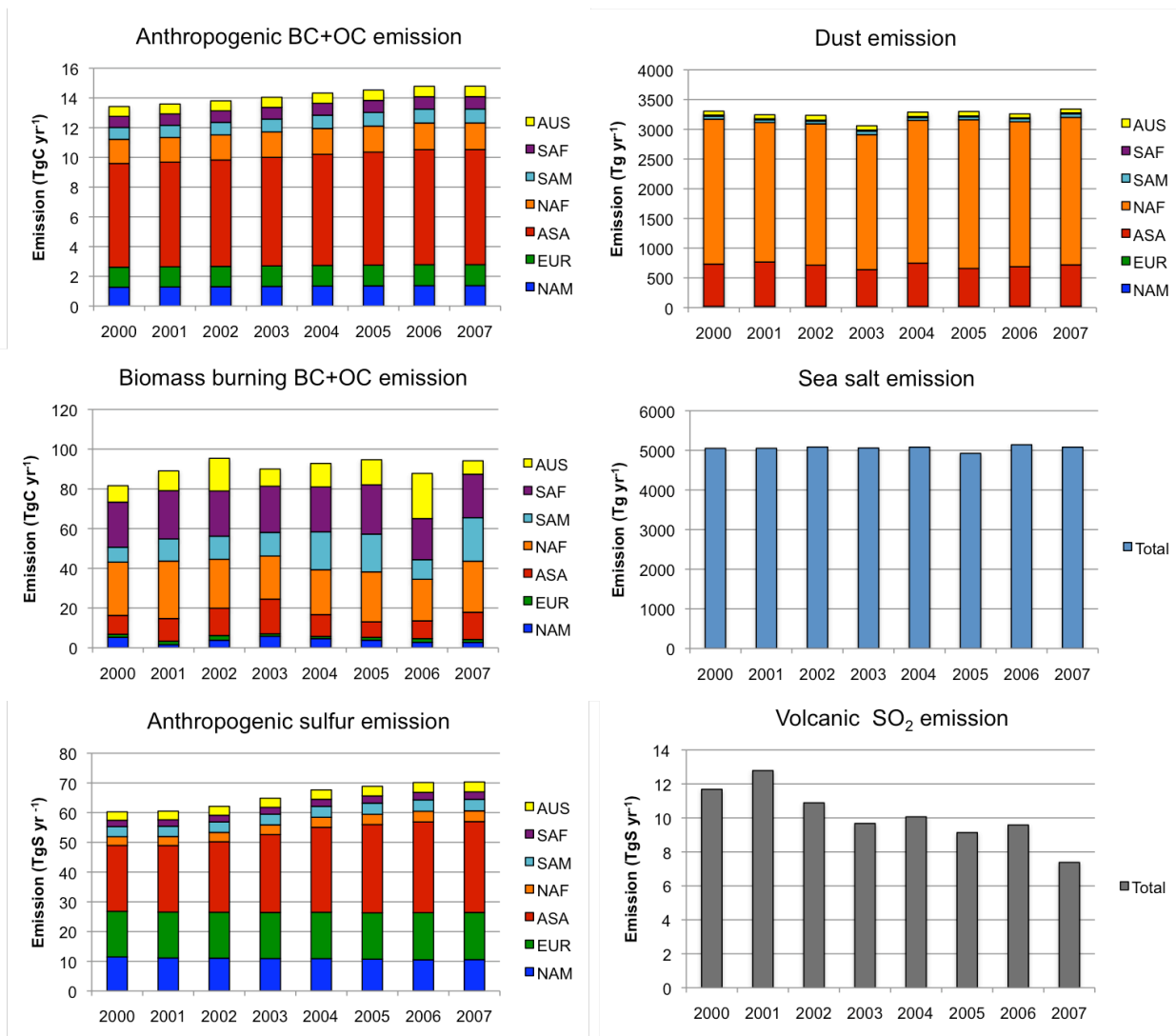


Figure 1. Emissions of aerosols and precursor gases from their major sources and source regions from 2000 to 2007, annual total amount. NAM = North America, EUR = Europe, ASA = Asia, NAF = northern Africa and Middle East, SAM = South America, SAF = southern Africa, AUS = Australia/New Zealand and countries in the tropical South Pacific. See Figure 4 for region domains.

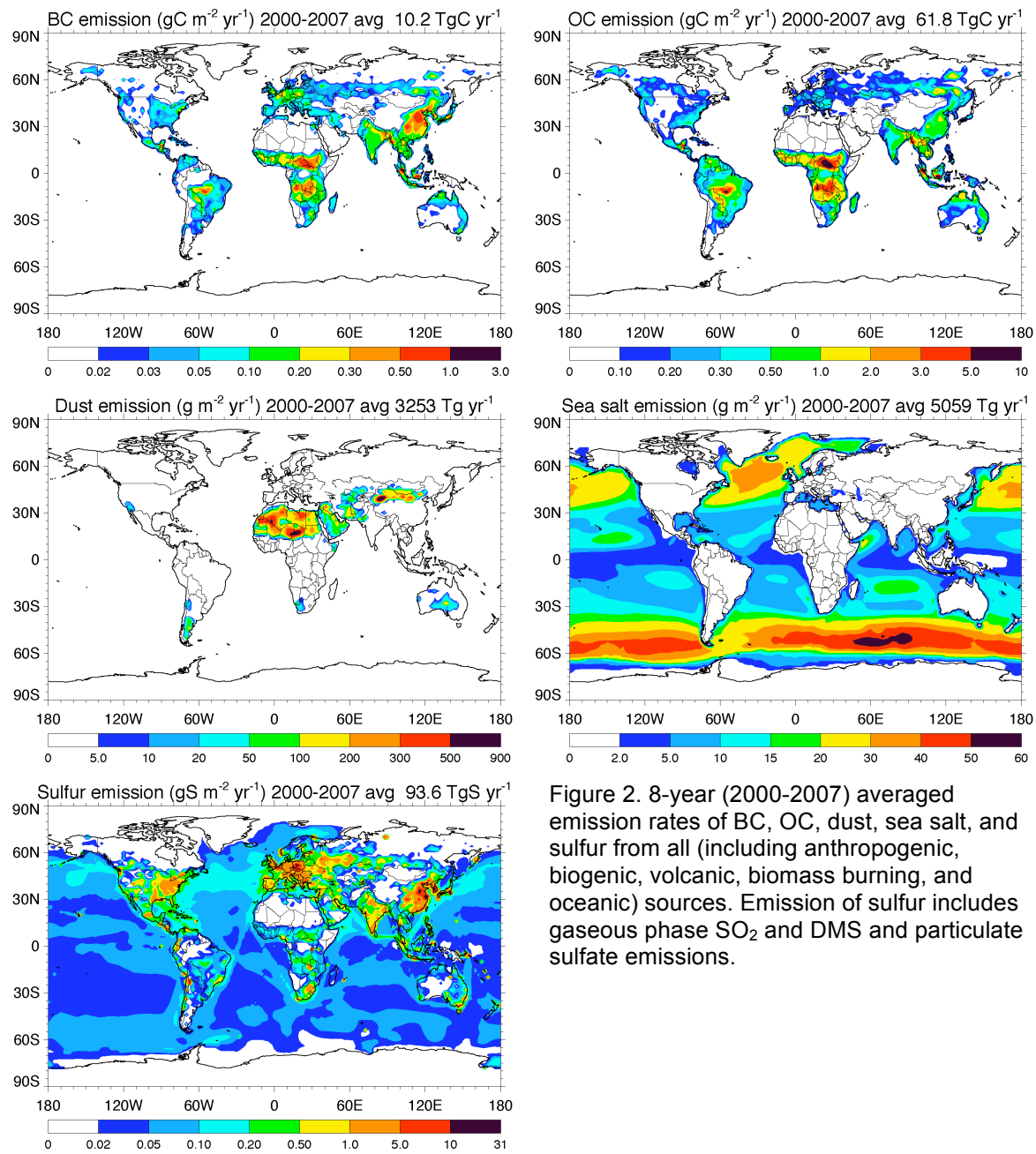


Figure 2. 8-year (2000-2007) averaged emission rates of BC, OC, dust, sea salt, and sulfur from all (including anthropogenic, biogenic, volcanic, biomass burning, and oceanic) sources. Emission of sulfur includes gaseous phase SO_2 and DMS and particulate sulfate emissions.

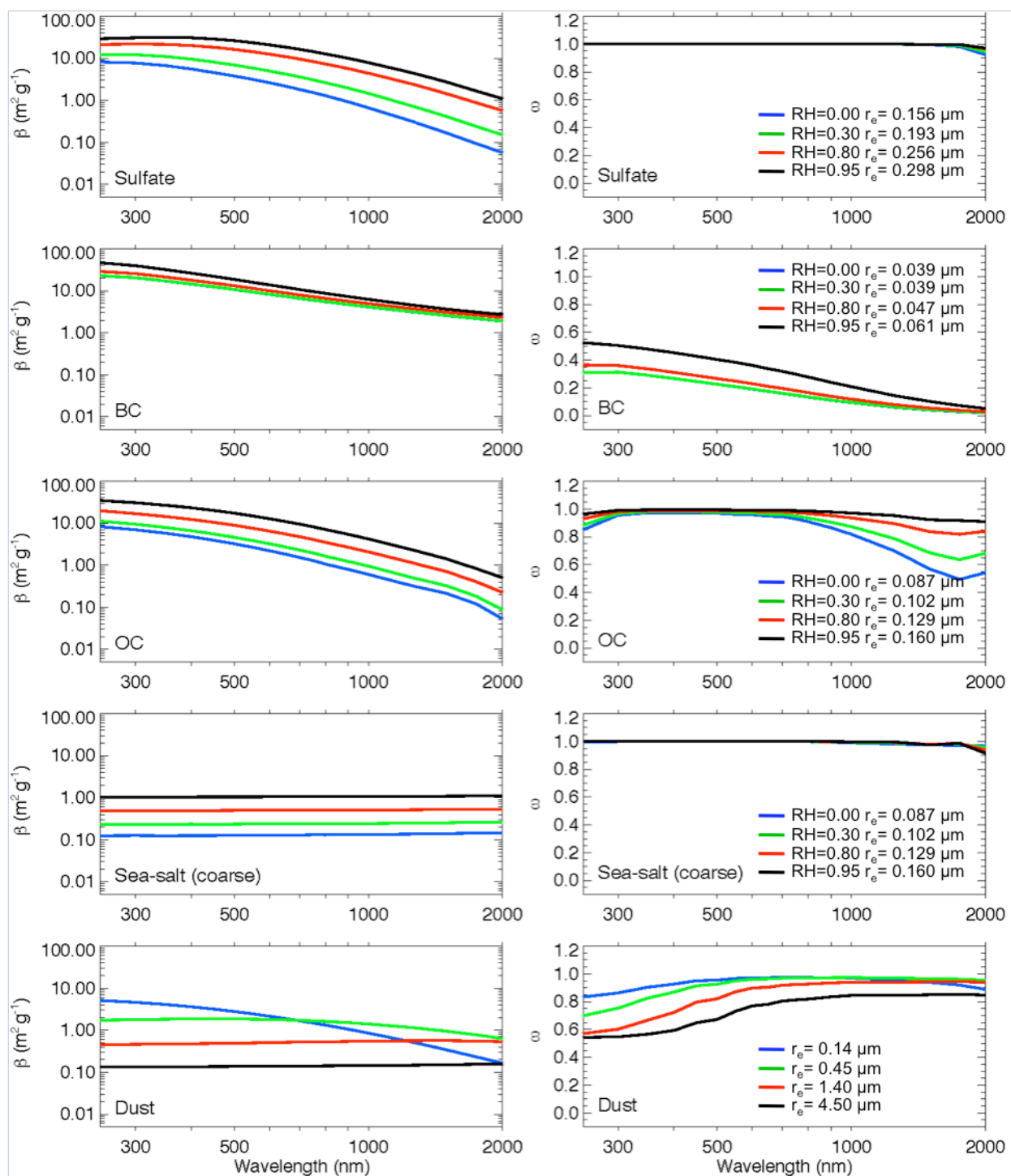


Figure 3. Mass extinction cross-section (aka mass extinction efficiency) β (left column) and single scattering albedo ω (right column) for sulfate, BC, OC, coarse sea salt, and dust as a function of wavelength from 250 to 2000 nm. Four different sizes of each species are shown with respective effective radius (r_e) at different RH values indicated in the panels in the right column.

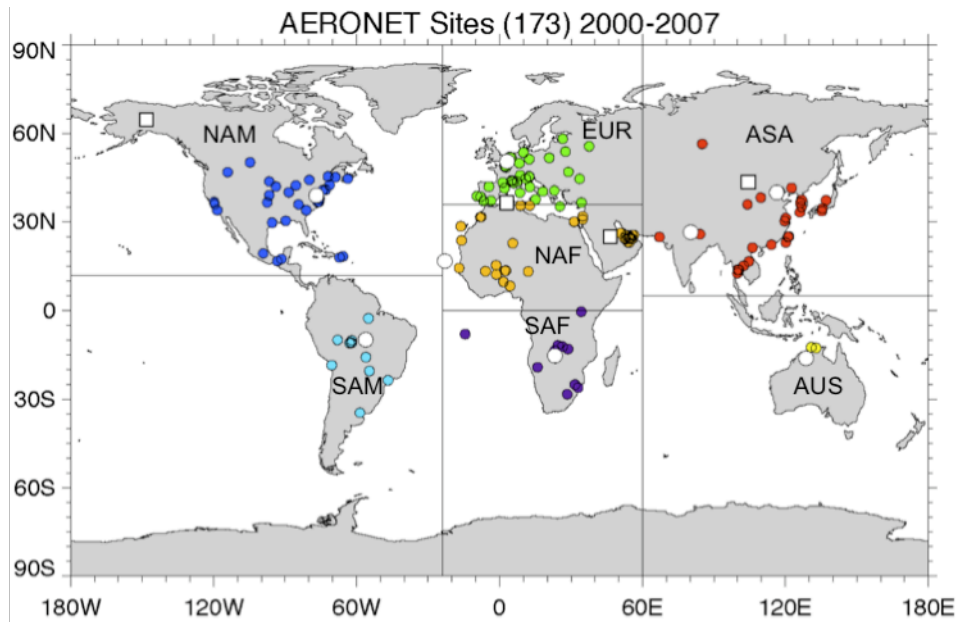


Figure 4. AERONET site locations where simultaneous τ and τ_a data are available for at least 20 days during 2000 to 2007 (total 173 sites). Eight sites in white circles are selected for detailed analysis shown in Figure 5 (GSFC, USA, 40.0°N, 76.8°W; Lille, France, 51.6°N, 3.1°E; Kanpur, India, 26.5°N, 80.2°E; Beijing, China, 40.0°N, 116.4°E; Cape Verde, Sal Island, 16.7°N, 22.9°W; Alta Floresta, Brazil, 9.9°S, 56.1°W; Mongu, Zambia, 15.3°S, 21.2°E; Lake Argyle, Australia, 16.1°S, 128.8°E). These sites together with another four sites in white squares (Bonanza Creek, USA, 64.7°N, 148.3°W; Blida, Algeria, 36.5°N, 2.9°E; Solar Village, Saudi Arabia, 24.9°N, 46.4°E; Dalanzadgad, Mongolia, 43.6°N, 104.4°E) are used for the spectral dependence analysis of ω in Figure 7.

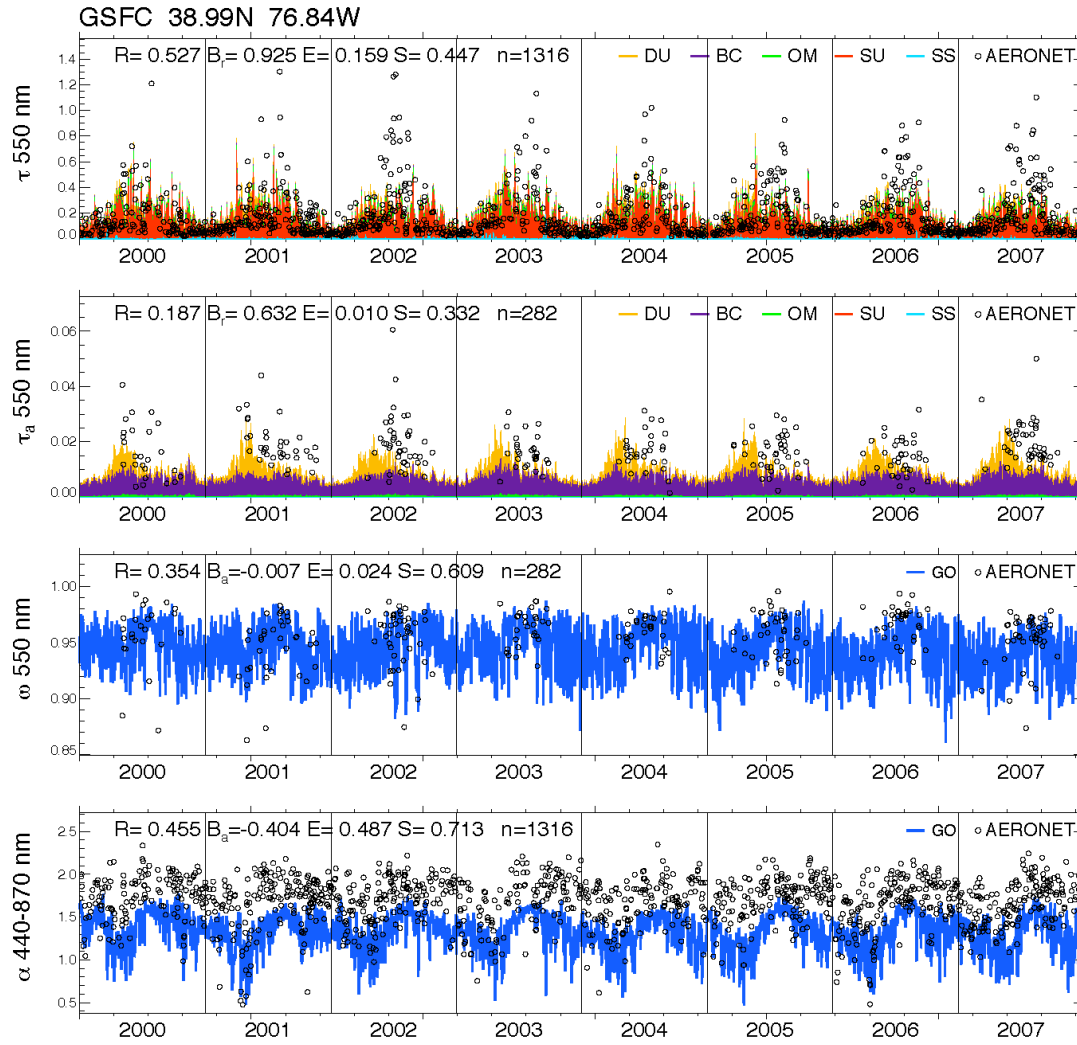


Figure 5a. Daily aerosol optical depth (τ , 1st panel), absorption optical depth (τ_a , 2nd panel), single scattering albedo (ω , 3rd panel) at 550 nm and Ångström exponent derived from τ at 440-870 nm (α , last panel) at Goddard Space Flight Center (GSFC) in eastern U.S.A. In the first two panels, GOCART aerosol components accumulated to total amount are shown in shaded color with DU=dust, BC=black carbon, OM=organic matter, SU=sulfate, and SS=sea salt. In the last two panels, model values are shown blue line with GO=GOCART. On each panel, R =correlation coefficient, B =bias with B_r in first two panels as relative mean bias, i.e. $\Sigma(\text{GOCART}_i)/\Sigma(\text{AERONET}_i)$ and B_a in the last two panels as absolute bias, i.e. $\Sigma(\text{GOCART}_i - \text{AERONET}_i)/n$ (n =total number of observations), E =root-mean-square error, and S =skill score. See text (section 3.2) for calculation of S .

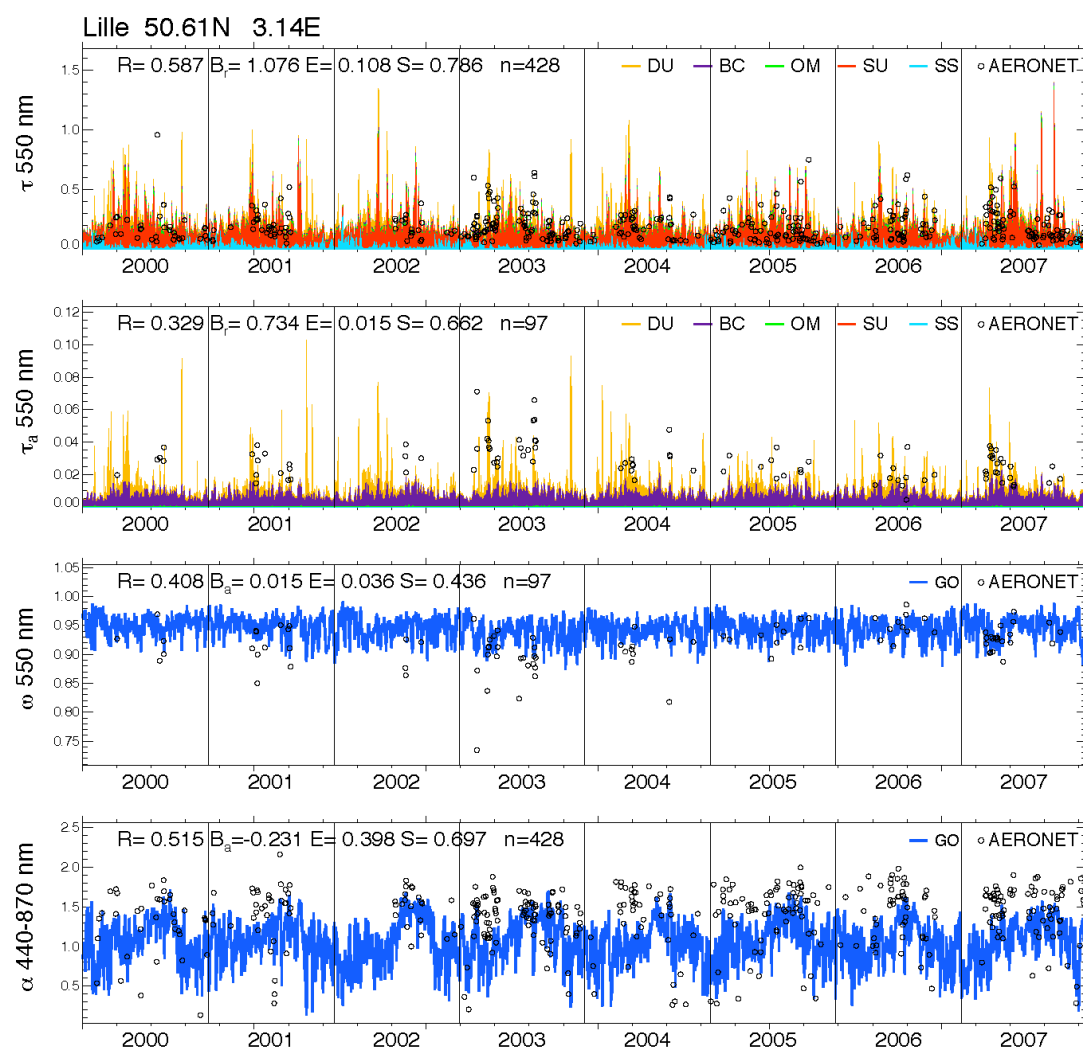


Figure 5b. Same as Figure 5a but for Lille, France.

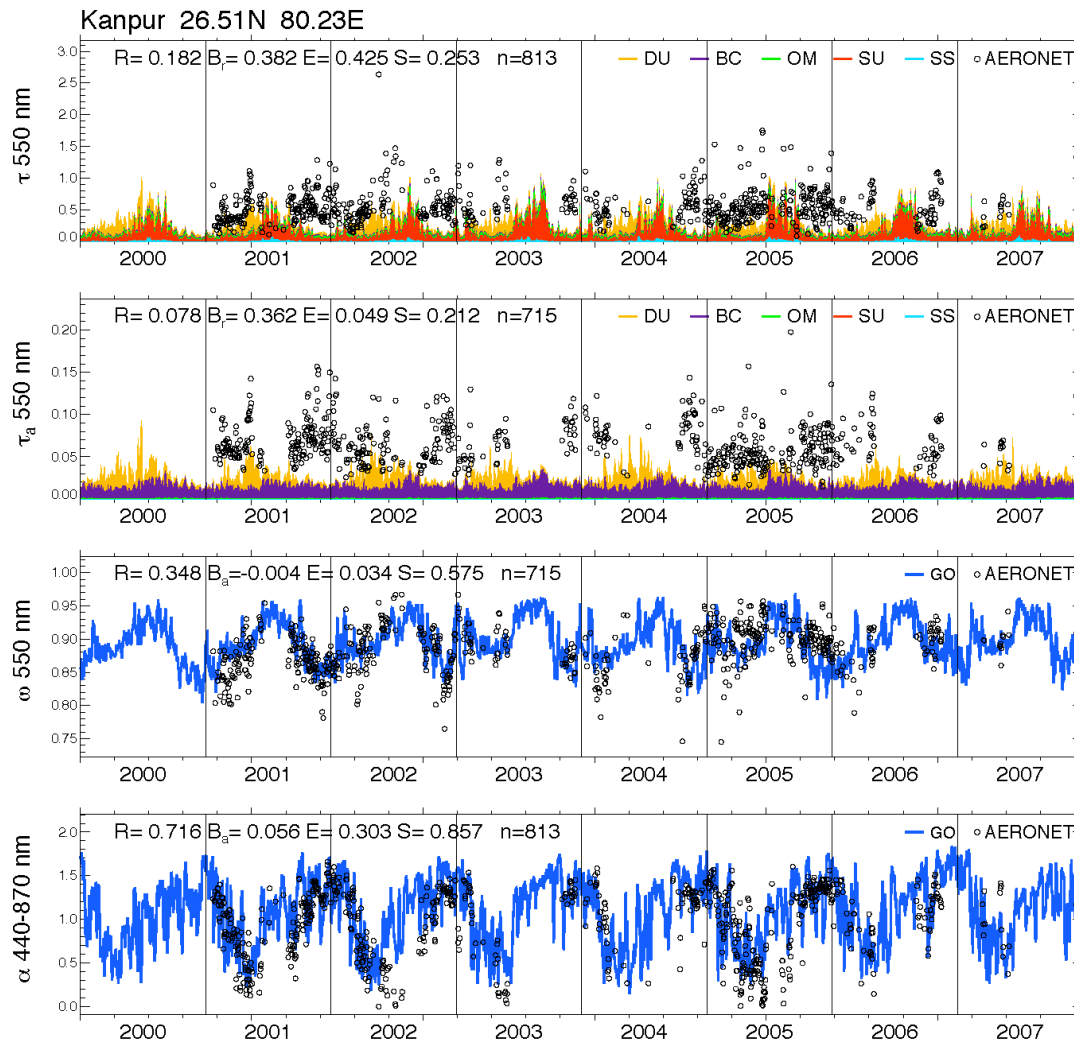


Figure 5c. Same as Figure 5a but for Kanpur, India.

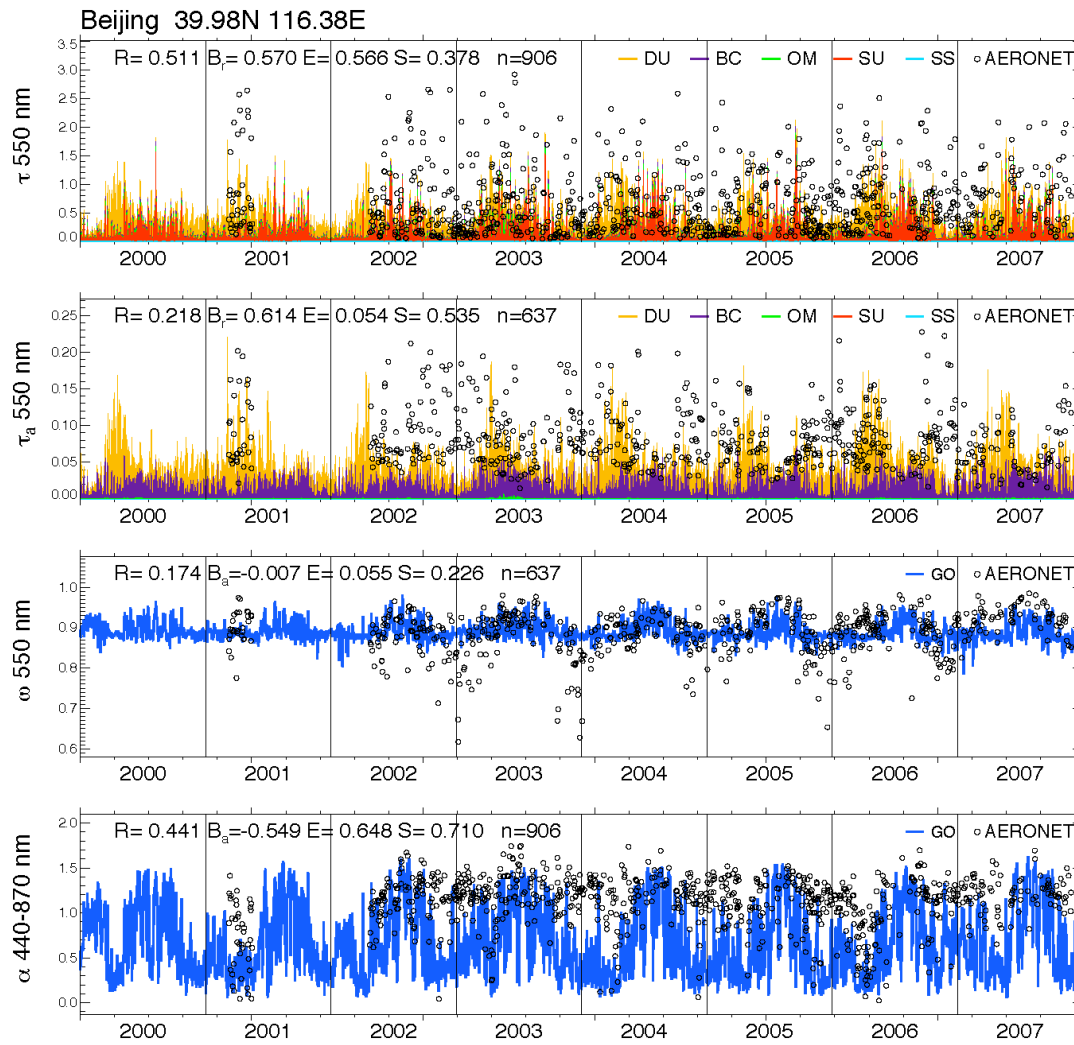


Figure 5d. Same as Figure 5a but for Beijing, China.

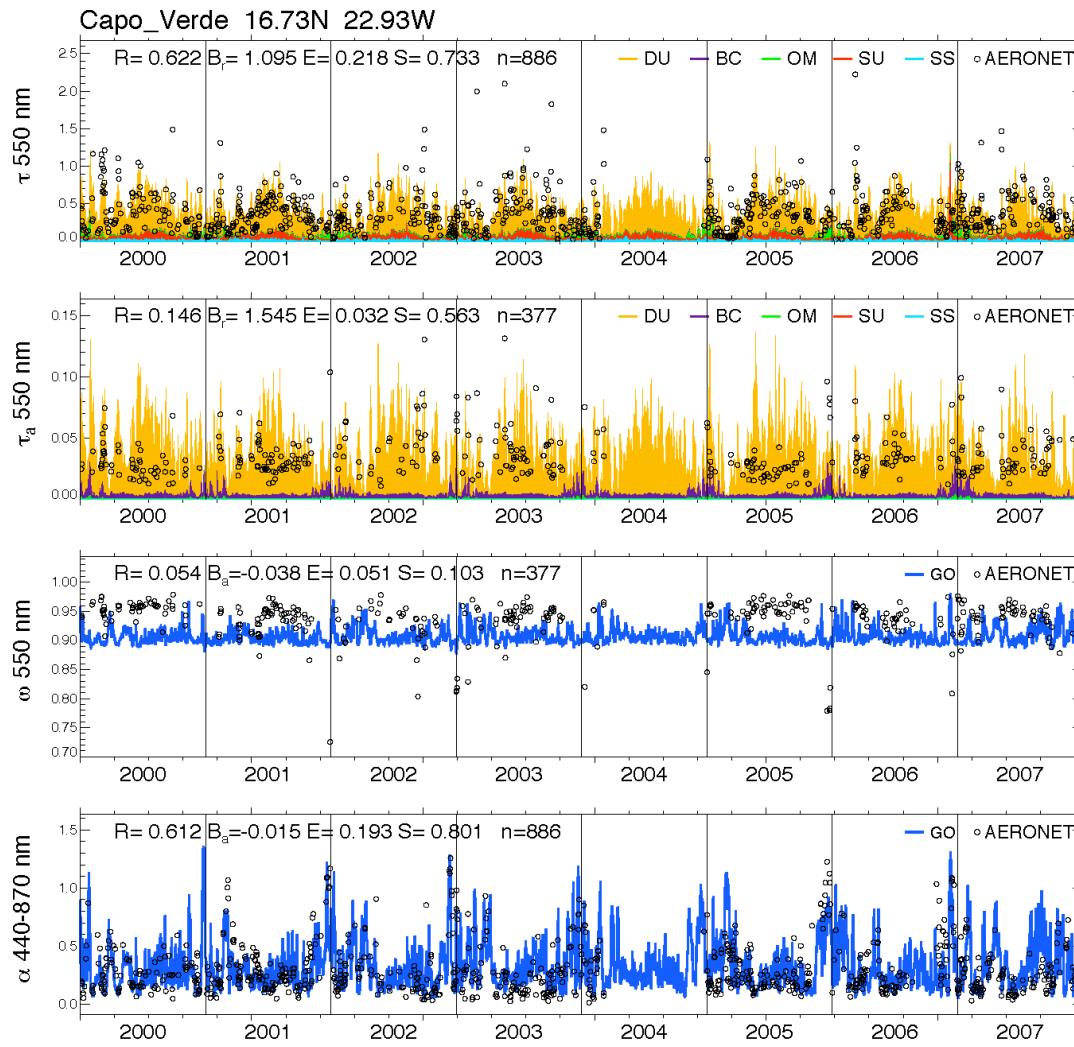


Figure 5e. Same as Figure 5a but for Cape Verde, off the west coast of northern Africa.

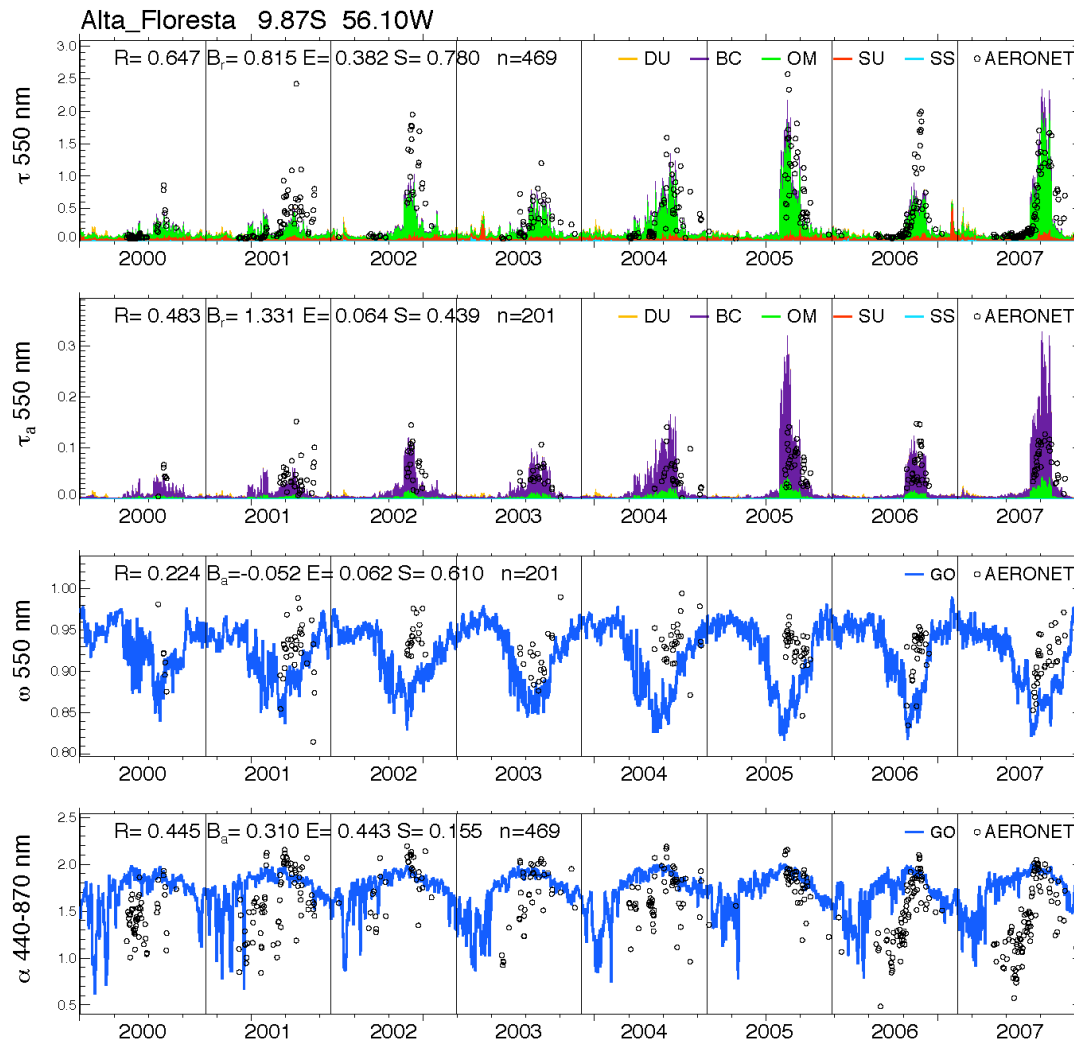


Figure 5f. Same as Figure 5a but for Alta Floresta in Brazil.

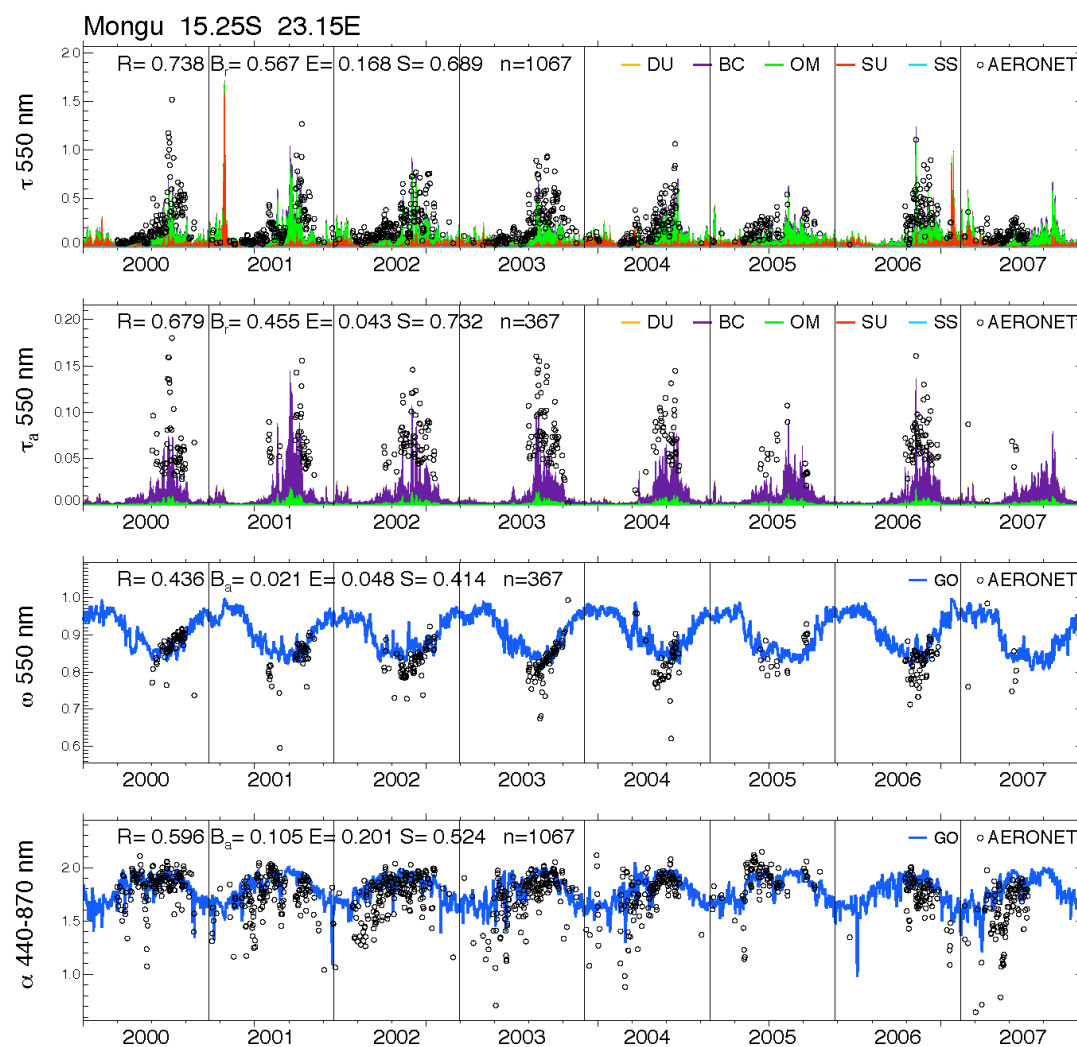


Figure 5g. Same as Figure 5a but for Mongu, Zambia.

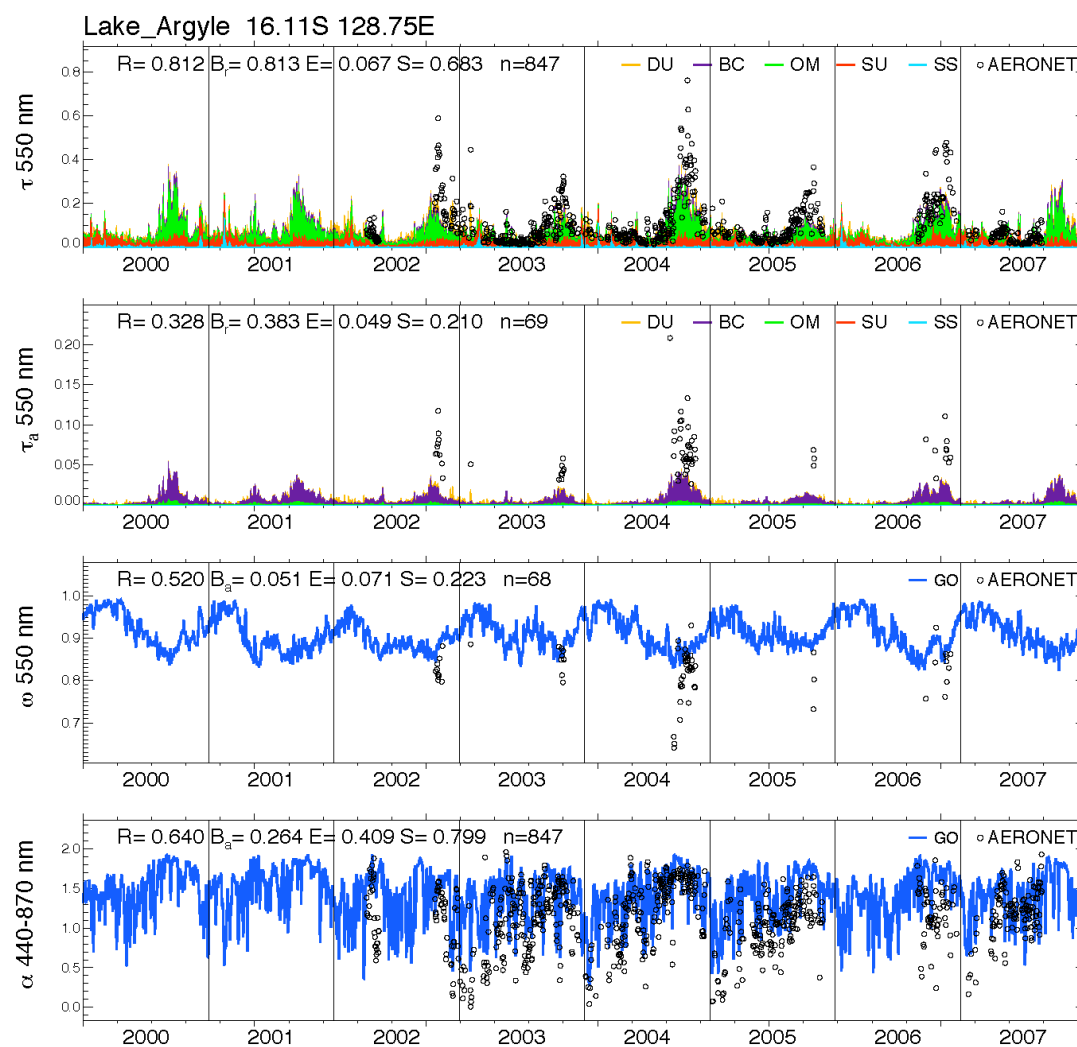


Figure 5h. Same as Figure 5a but for Lake Argyle in Australia.

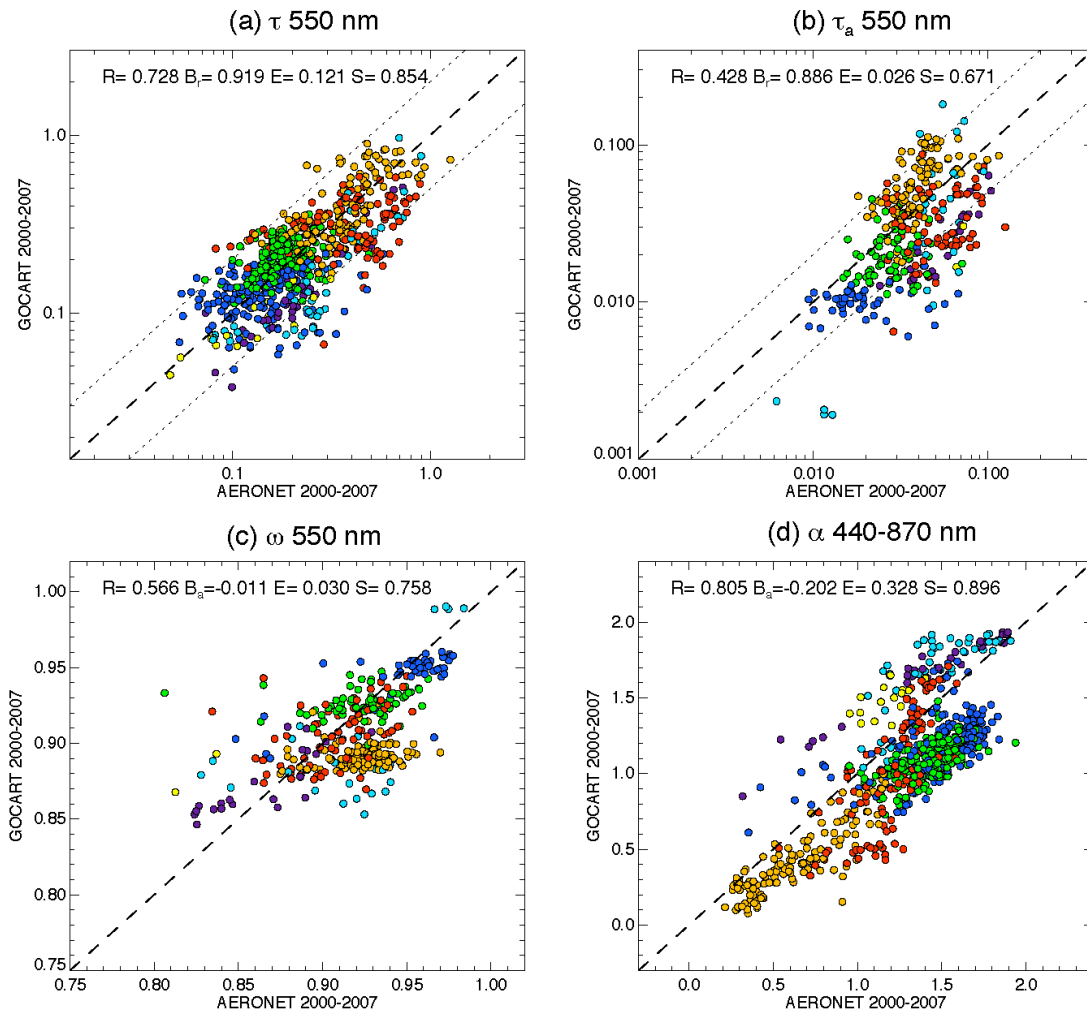


Figure 6. Overall comparisons of τ , τ_a , and ω at 550 nm and α at 440-870 nm between AERONET and GOCART at all 173 AERONET sites (see Figure 3) during 2000-2007. Each point represents the annual average of the available AERONET data with a year. Model output is averaged for the same days. Points are color coded according to the regions (see Figure 3). 1:1 ratio in dashed line and 2:1 in dotted lines on τ and τ_a panels. Statistical variables on each panel are: R =correlation coefficient, B_r =relative mean bias (for τ and τ_a), B_a =absolute mean bias (for ω and α), E =root-mean-square error, and S =skill score. See text and Figure 5a caption for explanations.

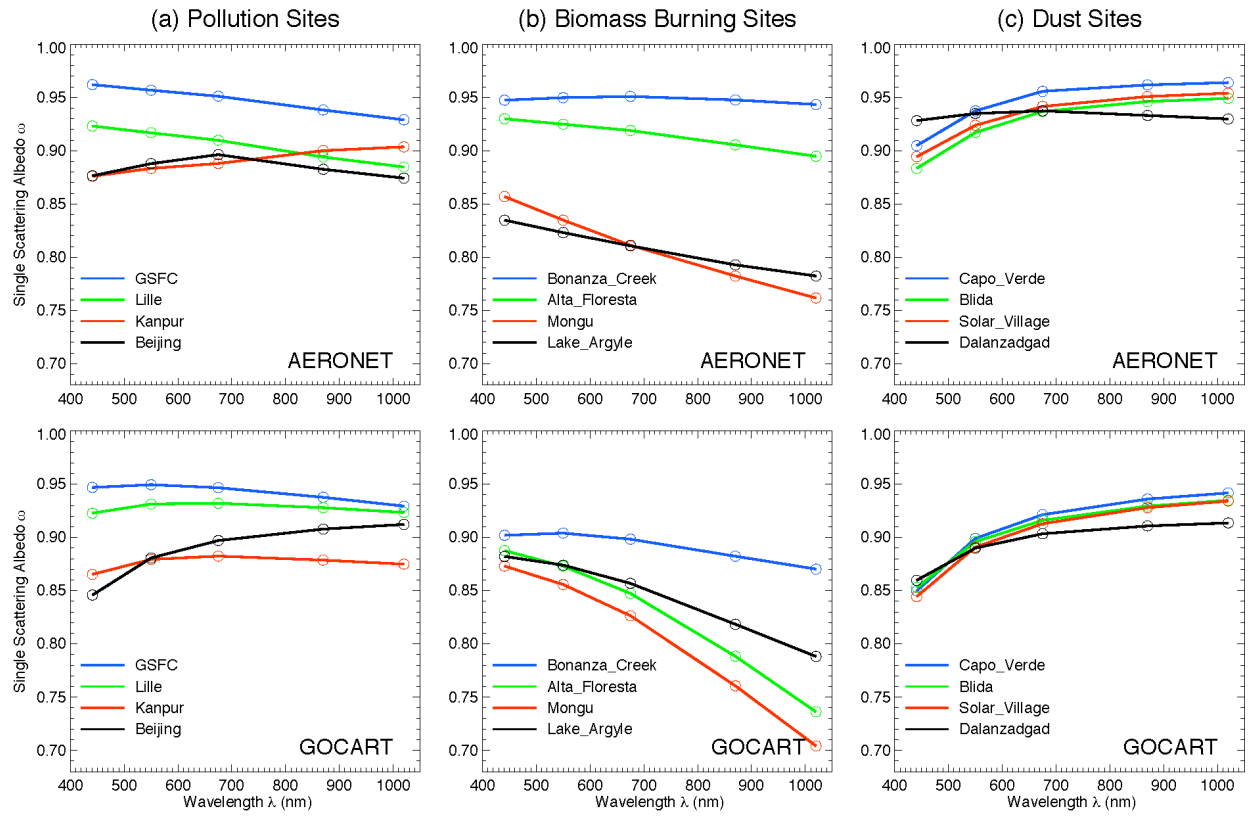


Figure 7. Spectral dependence of ω at four sites each located at (a) pollution, (b) biomass burning, and (c) dust regions as shown in the AERONET retrieval (top row) and GOCART model (bottom row). Points are averaged over all available daily data from AERONET retrievals from 2000 to 2007. Site locations are indicated in Figure 4 and discussed in the text.

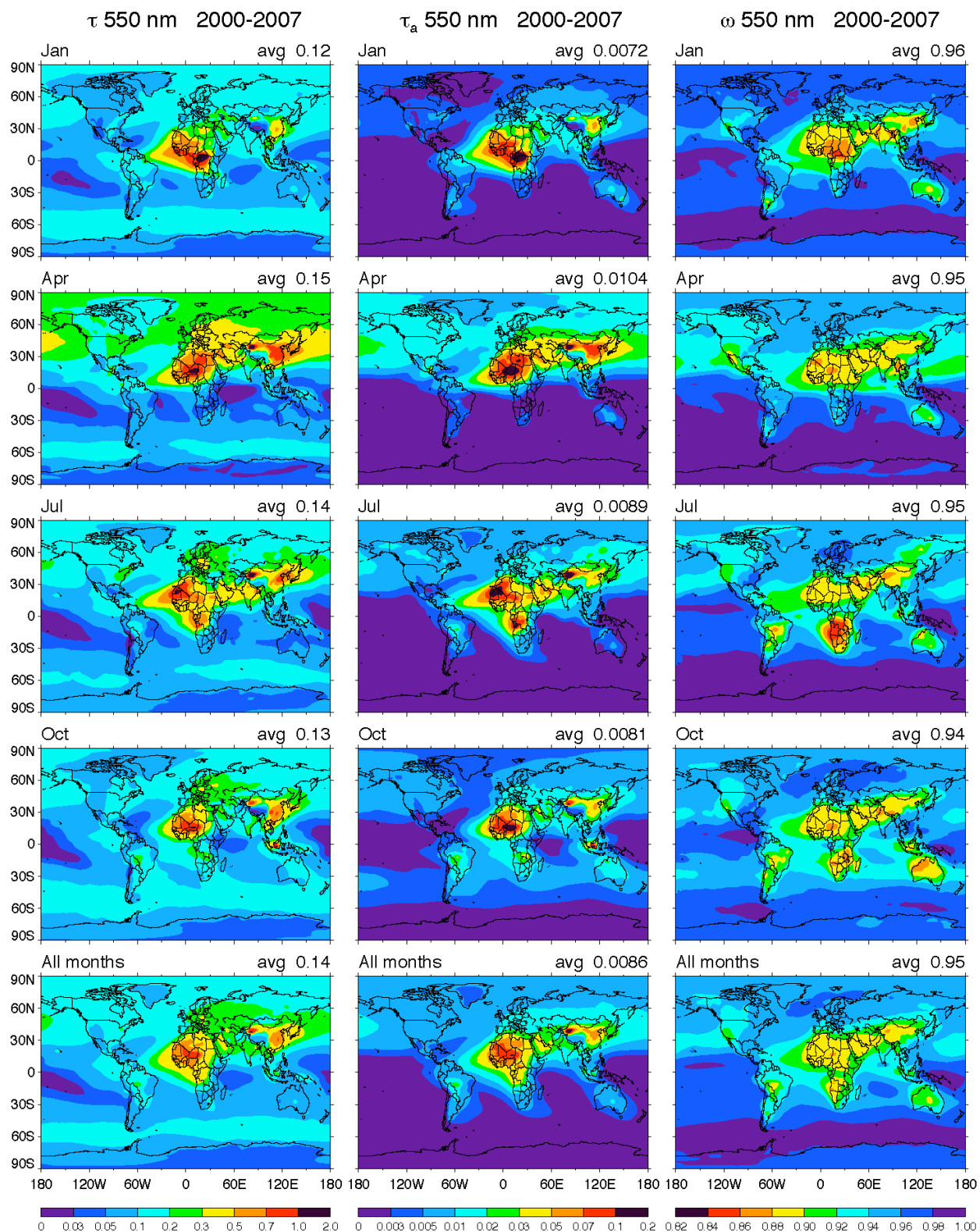


Figure 8. Global distributions of τ (left column), τ_a (middle column), and ω (right column) in January (1st row), April (2nd row), July (3rd row), and October (4th row) averaged over 8-year period from 2000 to 2007. The time averages of τ , τ_a , and ω for the entire 8-year period are shown in the last row.

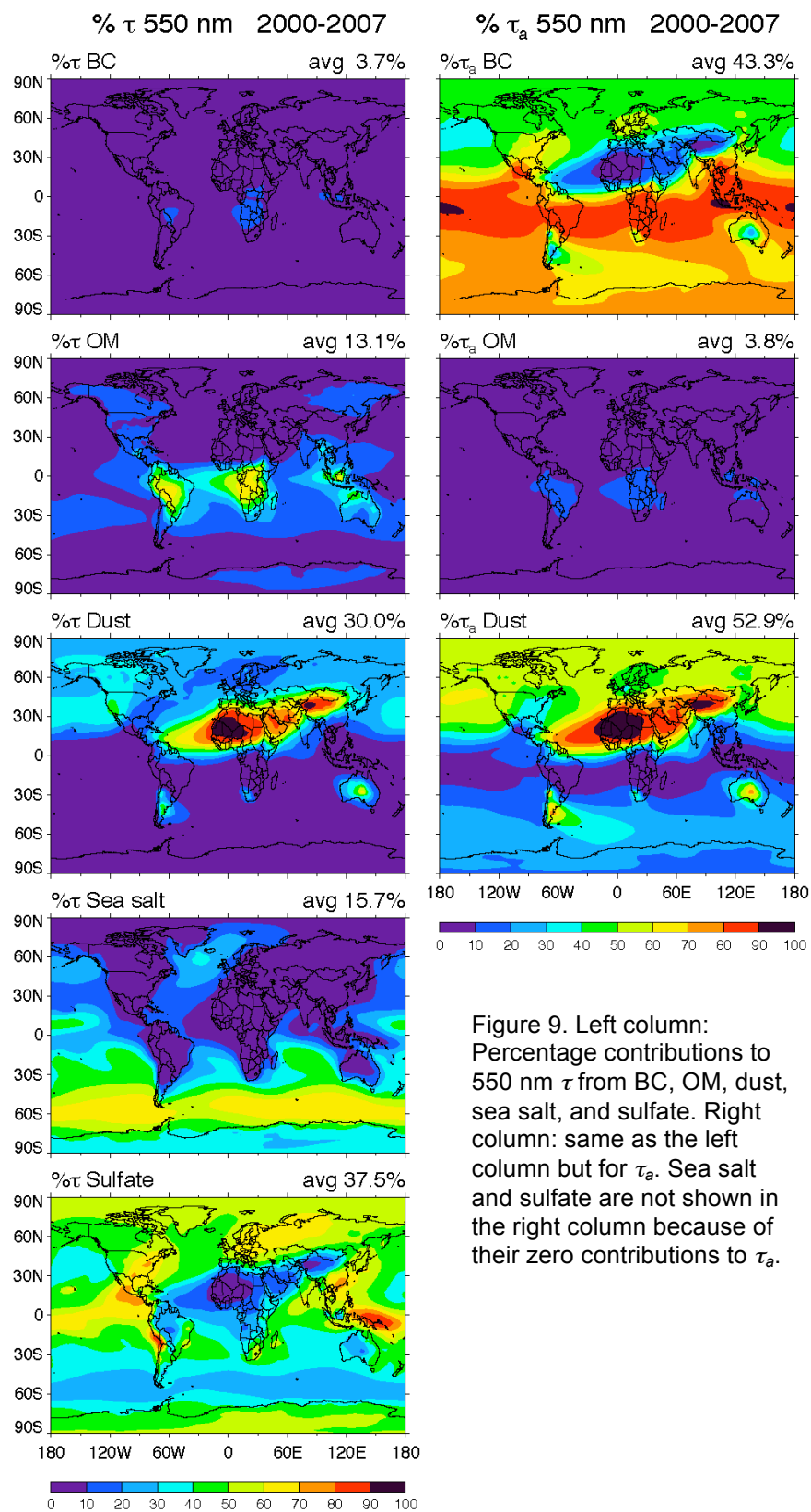


Figure 9. Left column: Percentage contributions to 550 nm τ from BC, OM, dust, sea salt, and sulfate. Right column: same as the left column but for τ_a . Sea salt and sulfate are not shown in the right column because of their zero contributions to τ_a .

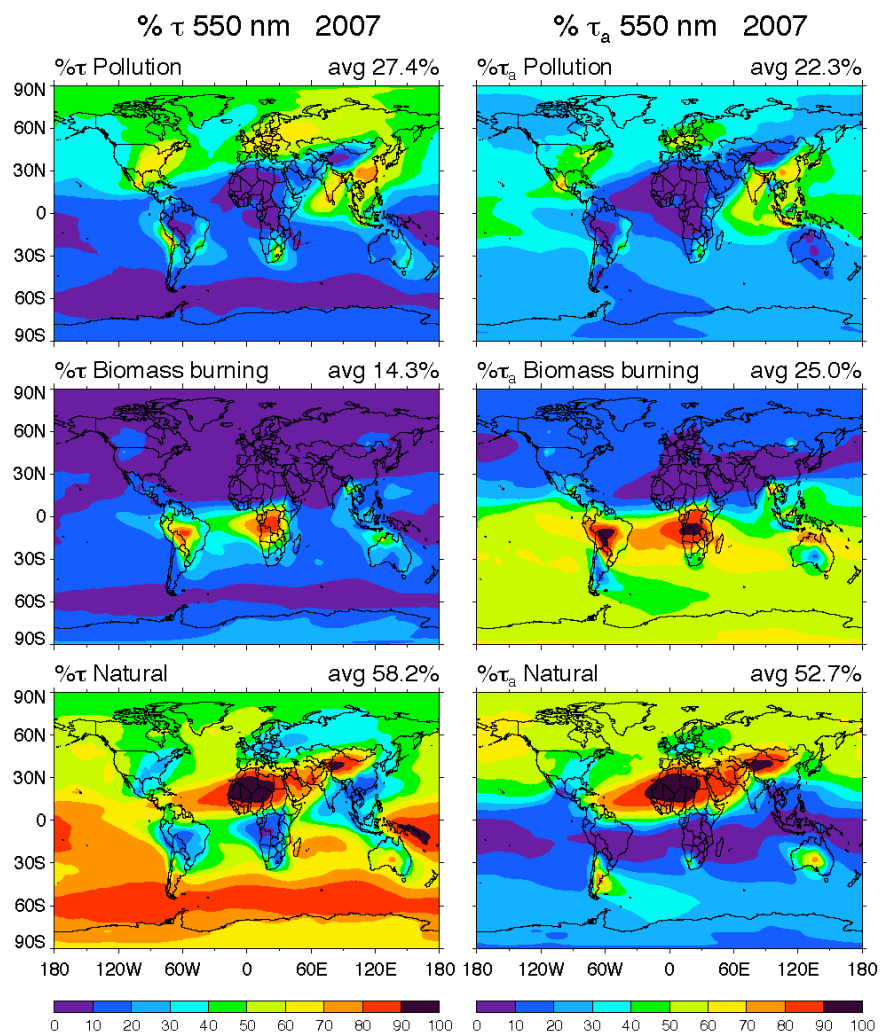


Figure 10. Percentage contributions to 550 nm τ (left column) and τ_a (right column) from pollution (top row), biomass burning (middle row), and natural (bottom row) aerosols in 2007. Natural aerosol including dust, sea salt, biogenic, and volcanic aerosols.